April 1997 • NREL/SR-520-22797

Processing of $CuInSe_2$-Based Solar Cells: Characterization of Deposition Processes in Terms of Chemical Reaction Analyses

Phase I Annual Report
6 May 1995 - 5 May 1996

T. Anderson
University of Florida
Gainesville, Florida

National Renewable Energy Laboratory
1617 Cole Boulevard
Golden, Colorado 80401-3393
A national laboratory of
the U.S. Department of Energy
Managed by Midwest Research Institute
for the U.S. Department of Energy
under Contract No. DE-AC36-83CH10093

NREL/SR-520-22797 • UC Category: 1260 • DE97000241

Processing of $CuInSe_2$-Based Solar Cells: Characterization of Deposition Processes in Terms of Chemical Reaction Analyses

Phase I Annual Report
6 May 1995 - 5 May 1996

T. Anderson
University of Florida
Gainesville, Florida

NREL technical monitor: B. von Roedern

National Renewable Energy Laboratory
1617 Cole Boulevard
Golden, Colorado 80401-3393
A national laboratory of
the U.S. Department of Energy
Managed by Midwest Research Institute
for the U.S. Department of Energy
under Contract No. DE-AC36-83CH10093

Prepared under Subcontract No. XAF-5-14142-10
April 1997

This publication was reproduced from the best available camera-ready copy submitted by the subcontractor and received no editorial review at NREL.

NOTICE

This report was prepared as an account of work sponsored by an agency of the United States government. Neither the United States government nor any agency thereof, nor any of their employees, makes any warranty, express or implied, or assumes any legal liability or responsibility for the accuracy, completeness, or usefulness of any information, apparatus, product, or process disclosed, or represents that its use would not infringe privately owned rights. Reference herein to any specific commercial product, process, or service by trade name, trademark, manufacturer, or otherwise does not necessarily constitute or imply its endorsement, recommendation, or favoring by the United States government or any agency thereof. The views and opinions of authors expressed herein do not necessarily state or reflect those of the United States government or any agency thereof.

Available to DOE and DOE contractors from:
Office of Scientific and Technical Information (OSTI)
P.O. Box 62
Oak Ridge, TN 37831
Prices available by calling (423) 576-8401

Available to the public from:
National Technical Information Service (NTIS)
U.S. Department of Commerce
5285 Port Royal Road
Springfield, VA 22161
(703) 487-4650

Printed on paper containing at least 50% wastepaper, including 20% postconsumer waste

Table of Contents

Summary 1
List of Figures 3
List of Tables 5
Introduction and Overview 6
Development of the Dual Beam Optical Modulation Technique 8
- Introduction 8
- Theory 9
  - Transmission Mode DBOM Measurement 9
  - Reflection Mode DBOM Measurement 12
- Experimental Aspects of DBOM Lifetime Measurement 14
- Results and Discussion 15
  - Validation and Exploration of DBOM Technique 15
    - Test of the Model's Linearity Prediction 15
    - Demonstration of Lifetime Variations Within CIS Films 17
    - Demonstration of Lifetime Variations Across CIS Films 19
    - Comparison of Transmission and Reflection Mode DBOM 19
  - Application to Device Structures and Processing 20
    - CdTe Solar Cells 20
    - Buffer and Window Layers on CIS 21
    - Buffer Layer Processing 22
- Summary 25
- References 25

Thermodynamic Assessment of the Cu-In-Se System 29
- Introduction 29
- Se System 30
- In-Se System 37
  - Assessment 37
  - Experimental Studies 43
- Cu-Se System 47
- Summary 49

References 49
Cell Fabrication Infrastructure Development 51
Plasma Migration Enhanced Epitaxy 51
CdS Deposition 53
Sputter Deposition of Mo and ZnO 53
Rapid Thermal Processing 55
Team Activities 57
Communications 59

SUMMARY

An interdisciplinary team of five graduate students and four faculty have made considerable progress during Phase I of this program. The objective of this initiative is to develop a high-rate processing sequence to produce device-quality thin films of CI(G)S(Se). A comprehensive CI(G)S(Se) device fabrication capability is being established that includes thermal evaporation and plasma assisted deposition of CI(G)S(Se), rapid thermal processing, DC sputtering of both undoped and doped ZnO, CBD and MOCVD of CdS, and rf sputtering of Mo. Insight into the materials processing issues is being addressed through assessment of the thermochemistry and phase equilibria of the CI(G)S(Se) system, single crystal growth studies, investigation of Na effects on the growth, and detailed materials characterization.

Specific accomplishments during Phase I include:

1. A nondestructive, contactless, dual-beam optical modulation (DBOM) technique was developed for measuring the excess carrier lifetimes and surface recombination velocities in CIGS. The method was tested in both a reflectance and transmission mode and a model was generated to interpret the data. Measurements on a sample in both modes gave measured lifetimes that agreed within experimental error. In a comparative study of the effects of CBD and MOCVD CdS on the measured lifetimes it was determined that both processes have beneficial effects. Furthermore, the results of this study suggested that a final bake in air is not required to achieve high lifetimes. The measured lifetimes correlated well with expected cell efficiency and a comparison of top-side and back-side illumination data on a CIS sample indicated a significant front surface recombination velocity (~ 10^5 cm/s). This technique was also used to study CdTe films.

2. Critical assessments of the Se unary and the In-Se and Cu-Se binary systems were performed. The results of the Se assessment indicated that the dominant species are Se_2 for T > 1000 K, Se_5 in the range 600 < T < 1000 K, and Se_6 for T < 600 K. Equilibrium evaporation fluxes were estimated using the assessed thermochemical properties. The first assessment of the In-Se system was performed and several inconsistencies were noted. To supplement the database for In-rich compounds, the Gibbs energy of formation of InSe, In_6Se_7, and In_2Se, and the activity

of In in melts were measured by a solid state galvanic cell technique. Finally, a preliminary assessment of the Cu-Se system was performed.

3. A cell fabrication infrastructure was established. The Plasma Migration Enhanced Epitaxy (PMEE) system was transferred from Boeing and initial calibration runs were performed. In addition we have installed and demonstrated a capability for rf sputtering of Mo, CBD and MOCVD of CdS, and RTP of Mo/glass and Cu-Se/Mo/glass.

4. Our team has participated in the CIS teaming efforts (B. Stanbery, S. Li and T. Anderson) and initiated a collaboration with Richard Anderson (Sandia California) under the auspices of the DOE Office of Basic Energy Science.

LIST OF FIGURES

Figure 1. (a) Schematic of the transmission mode DBOM apparatus
(b) Geometric construction used in the theory

Figure 2. (a) Schematic of reflection mode DBOM apparatus
(b) Geometric construction used in the theory

Figure 3. (a) The linear relationship of $\Delta I/I$ for NREL sample CIS (S670-C23S)
(b) The linear relationship of $\Delta I/I$ for NREL sample CIGS (S670-C14S)

Figure 4. The linear relationship of $\Delta I/I$ under front-side illumination for both the He-Ne and He-Cd laser

Figure 5. Areal mapping of τ_{eff} (ns) measured by transmission mode DBOM technique (USF sample C71-2-1, CIS/Mo)

Figure 6. Processing sequence for the 4 NREL CIGS samples

Figure 7. Box plot of lifetime data statistical summary from buffer layer processing

Figure 8. The spatial distribution of the excess carrier lifetime τ_{eff} (ns) for NREL CIGS samples C498-1 and C498-4

Figure 9. The spatial distribution of the excess carrier lifetime τ_{eff} (ns) for NREL CIGS samples M1414-2 and M1414-3

Figure 10. Comparison between experimental and assessed total pressure over solid Se from 298 to 494 K

Figure 11. Comparison between the experimental and assessed total pressure over liquid Se from 494 to 1500 K

Figure 12. Assessed total and partial pressures over solid Se from 298 to 494 K

Figure 13. Assessed total and partial pressures over liquid Se from 494 to 1500 K

Figure 14. The calculated free evaporative $Se_n(g)$ flux above liquid selenium

Figure 15. Assessed In-Se temperature-composition phase diagram

Figure 16. Equilibrium $In_2Se(g)$ and $Se_2(g)$ partial pressure over $In_2Se_3(s)$

Figure 17. Equilibrium Se_2 and In partial pressure over $In_2Se_3(s)$ liquidus

Figure 18. Predominance diagram for the In-Se system

Figure 19. Experimental determination of the indium activity in In-Se melts with solid-state galvanic cells

Figure 20. Assessed T-x phase diagram for In-Se system

Figure 21. Assessed Cu-Se temperature-composition phase diagram

Figure 22. Schematic of the plasma migration enhanced epitaxy system

Figure 23. AFM micrograph of sputtered Mo film on glass

LIST OF TABLES

Table 1. Optical and dielectric parameters used in model.

Table 2. Excess carrier lifetime for 2 samples measured in transmission mode.

Table 3. The excess carrier lifetime of a USF CIS sample measured by transmission DBOM under front- and back-side illumination at two wavelengths.

Table 4. Comparison between transmission and reflection mode measured lifetimes.

Table 5. Average measured excess carrier lifetime for CdTe samples.

Table 6. Average excess carrier lifetime in CIS samples measured in reflection mode.

Table 7. Average excess carrier lifetime in CIGS samples measured in reflection mode.

Table 8. Optimized values of the Gibbs energy relative to H_{SER} of Se species. The gas phase species are at a standard vapor pressure of 1 atm.

Table 9. Optimized Gibbs energy espressions for compounds in the In-Se system.

Table 10. Phase analysis in annealed In-Se alloys.

Table 11. Lattice structures of the compounds identified in the In-Se system.

INTRODUCTION

A diverse team of researchers has been assembled at the University of Florida to investigate the processing of $CuInSe_2$-based (CIS) photovoltaics (PV). The over-arching purpose of this project is to substantiatively contribute to the full commercialization of CIS-based PV technology. To this end, two tracks of research have been initiated: 1) develop and understand deposition and annealing processes that will lead to reduced manufacturing costs and 2) contribute to our basic understanding of the material properties of CIS and junction formation.

With respect to the first track of research, the team is investigating a processing sequence that involves the initial growth of a highly ordered structural template at relatively low rate, followed by the rapid deposition of the bulk of the absorber film's mixed-phase precursor using a plasma-assisted deposition technique, and then finish with Rapid Thermal Processing (RTP) to recrystallize the film from the seed layer. The high rate deposition utilizes an Electron Cyclotron Resonance (ECR) plasma selenium source to reduce deposition temperature, ensure efficient incorporation of selenium in the film, and provide a driving force at the surface to overcome kinetic limitations of thermal growth at high deposition rate. Through our participation on the CIS teams organized by NREL as part of the Thin Film Partnership Program, we also are exploring an alternative process (MOCVD) to deposit buffer layers (ZnCdS), as well as a Cd-free buffer layer (e.g., ZnS). Finally, we are exploring a potentially lower-cost, manufacturable process for conductive, transparent ZnO "window" layer deposition based on DC sputtering from metallic zinc targets using boron or silicon doping. Materials characterization is essential to achieving an understanding of the relations between processing and device performance characteristics. The team is using a variety of characterization techniques to gain insight on these relations, including the development of a new nondestructive and contactless method for measuring effective carrier lifetimes in CIS films (Dual-Beam Optical Modulation: DBOM).

The second tract of research focuses on fundamental issues related to CIS processing. Specifically, the thermochemistry and phase equilibria in the Cu-In-Se system is being rigorously assessed using the CALPHAD approach and critical missing data are being measured. The outcome of this research will be a full description of the ternary phase diagram that will be useful

for optimizing the deposition and annealing processes, suggesting alternative precursor film compositions, and understanding the junction formation process.

A second thread of fundamental research is the growth of single crystal CIS films. Although this approach is not expected to be commercially feasible, it will assist in establishing performance benchmarks and permit us to exclude the influence of extended defects and multiple phases on device performance. High crystalline quality films will be grown at low temperature on single crystal substrates by migration enhanced epitaxy (MEE). These investigations will provide a detailed understanding of the role of ordered phases at junctions and the effect of "contaminants" such as sodium on the growth kinetics of $CuInSe_2$.

During Phase I of the project considerable progress has been achieved in establishing the necessary device processing infrastructure. We have successfully transferred from Boeing and further developed the MEE deposition system, constructed and tested the RTP system, demonstrated CBD and MOCVD growth of CdS, and performed initial Mo and ZnO sputter depositions. We also have made good progress in two areas that are not dependent on the CIS deposition capability: development of the DBOM technique and the thermodynamic assessment effort.

A strength of the program is the diversity in backgrounds of students and faculty team members. The graduate students include Ph.D. candidates B. Stanbery (formerly with Boeing) working on the CIS deposition process and C. Chang performing the CdS deposition and the assessment work with the help of post-doctoral associate A. Davydov (formerly assistant professor of chemistry at Moscow State University). L. Reith (Materials Science and Engineering) spent the 1995 summer at NREL and is working on sputter deposition of ZnO and Mo, while J. Desroches (Materials Science and Engineering) has developed the RTP system. C. Huang (Electrical Engineering) has had responsibility for applying the DBOM technique. The faculty team is comprised of 4 faculty from 3 departments: T. Anderson (Chemical Engineering), P. Holloway and K. Jones (Materials Science and Engineering) and S. Li (Electrical Engineering).

DEVELOPMENT OF THE DUAL BEAM OPTICAL MODULATION TECHNIQUE

Introduction

$CuInSe_2$ (CIS) or $CuInGaSe_2$ (CIGS) thin film solar cells have recently achieved conversion efficiencies approaching 18% AM1.5 [1]. To accelerate the further optimization of the device performance, however, a detailed study and a better understanding of the effects of processing on the CdS/CIS interface and CIS film transport properties is needed.

The performance (conversion efficiency, open-circuit voltage, short-circuit current) of a CIS solar cell is directly related to recombination parameters such as minority carrier lifetimes in the CIS films. Some diagnostic techniques have been employed for the characterization of structural properties in the CIS films [2,3], but development of a simple nondestructive contactless diagnostic technique for the determination of the excess carrier lifetimes in the CIS films would be an invaluable tool for optimizing the material parameters and fabrication process. In the past year we have demonstrated both transmission mode and reflection mode Dual Beam Optical Modulation (DBOM) techniques to directly measure the excess carrier lifetimes in CIS and CIGS films.

The reflection mode DBOM technique was applied to study the effects of the CdS buffer layer processing on the excess carrier lifetimes in CIGS films. Progress was achieved in extending the theoretical basis for transmission mode DBOM to reflection mode DBOM, the deposition of CdS layers on CIGS films by both CBD and MOCVD, and the measurement of excess carrier lifetimes in CdS/CIGS, ZnO/CdS/CIS and CdTe films.

Theory

The contactless DBOM technique is based on the modulation of the transmitted intensity of an infrared (IR) probe beam by a visible pump beam which causes free carrier absorption in the CIS film. The fractional change in the transmitted intensity of the IR probe beam is directly proportional to the effective excess carrier lifetime in the CIS films. Thus, the DBOM technique can be used to determine the excess carrier lifetimes in CIS films. In addition, the DBOM technique allows areal mapping of the excess carrier lifetimes across the CIS film with a spatial resolution of about 2 mm using our present apparatus. We have also demonstrated the technique's ability to perform depth profiling of excess carrier lifetimes in the film by changing the wavelength (and hence the absorption depth in the film) of the pump beam.

(1) Theory of the Transmission Mode DBOM Measurement

The DBOM technique was first developed for the characterization of excess carrier lifetimes in SOI materials using a transmission mode of operation [4]. We have also used the transmission mode DBOM technique for measurement of the excess carrier lifetimes in CIS films deposited on a semi-transmitting Mo coated glass substrate.

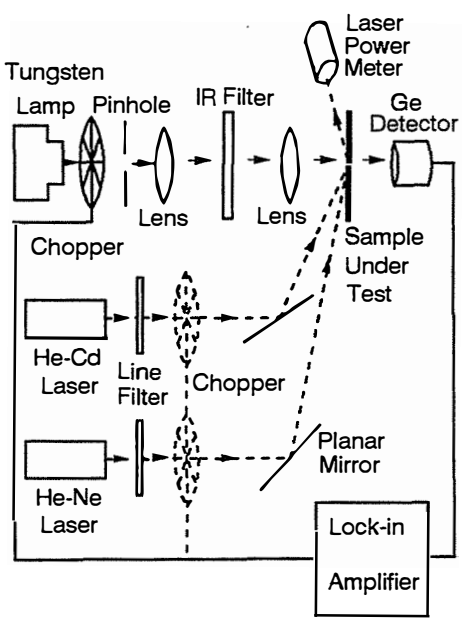

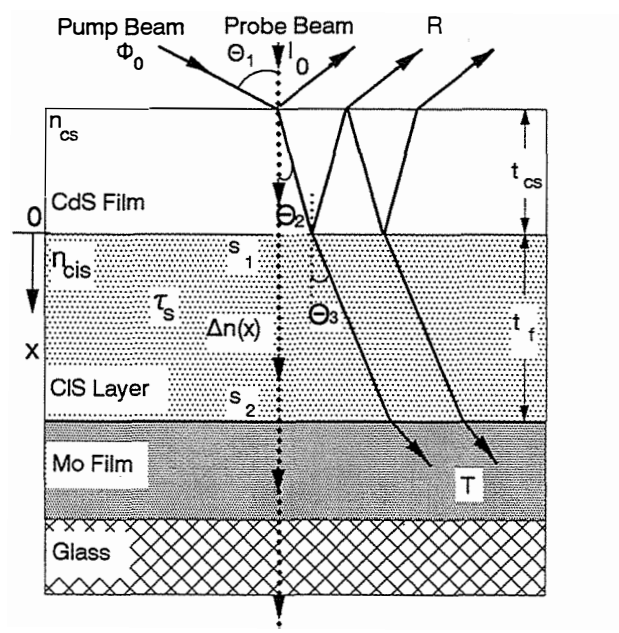

Figure 1. **(a) Schematic of the transmission mode DBOM apparatus** **(b) Geometric construction used in the theory**

Figure 1a shows a schematic diagram of the transmission mode DBOM experimental setup, while figure 1b shows the direction of the pump beam impinging on the CIS film. The excess electron density generated by the pump beam in the CIS layer can be obtained by solving the continuity equation for electrons and using the boundary conditions at the top (x = 0) and bottom interface ($x = t_f$) of the CIS film, which are given by

$$D_n \frac{\partial^2 \Delta n}{\partial x^2} - \frac{\Delta n}{\tau} + G(x) = 0 \tag{1}$$

$$D_n \left. \frac{\partial \Delta n}{\partial x} \right|_{x=0} = s_1 \Delta n(0) \tag{2}$$

$$-D_n \left. \frac{\partial \Delta n}{\partial x} \right|_{x=t_f} = s_2 \Delta n(t_f) \tag{3}$$

and the generation rate can be expressed as:

$$G(x) = \alpha \phi_0 \cos\theta_3 (1 - R - T) e^{-\alpha x} \tag{4}$$

where α, ϕ_0, R, and T are the absorption coefficient, photon flux, total front surface reflectance, and back-interface transmittance at a given pump beam wavelength, while D_n, t_f, τ, s_1, and s_2 are the diffusion coefficient, CIS film thickness, excess carrier lifetime, front-surface recombination velocity and back-interface recombination velocity in the CIS films, respectively.

The excess electron density in the CIS film as a function of distance along x-direction can be obtained by solving equation (1) subject to the boundary conditions given by equations (2) and (3), and the result yields

$$\Delta n(x) = \frac{\alpha \phi_0 (1 - R - T) \cos\theta_3}{D_n \left(\alpha^2 - \frac{1}{L_n^2} \right)} \left(C_1 e^{\frac{x - t_f}{L_n}} + C_2 e^{\frac{x - t_f}{L_n}} - e^{-\alpha x} \right) \tag{5}$$

where

$$C_1 = \frac{(\alpha D_n + s_1)\left(\frac{D_n}{L_n} - s_2\right) - (\alpha D_n - s_2)\left(\frac{D_n}{L_n} - s_1\right)e^{-[t_f(\alpha - 1/L_n)]}}{2\left[\frac{D_n}{L_n}(s_1 + s_2)\cosh\left(\frac{t_f}{L_n}\right) + \left(s_1 s_2 + \frac{D_n^2}{L_n^2}\right)\sinh\left(\frac{t_f}{L_n}\right)\right]} \tag{6}$$

$$C_2 = \frac{(\alpha D_n + s_1)\left(\frac{D_n}{L_n} + s_2\right) - (\alpha D_n - s_2)\left(\frac{D_n}{L_n} - s_1\right)e^{-[t_f(\alpha + 1/L_n)]}}{2\left[\frac{D_n}{L_n}(s_1 + s_2)\cosh\left(\frac{t_f}{L_n}\right) + \left(s_1 s_2 + \frac{D_n^2}{L_n^2}\right)\sinh\left(\frac{t_f}{L_n}\right)\right]} \tag{7}$$

The variable θ_3 is the internal propagation angle of the incident pump beam in the CIS layer to the normal, $L_n = (D_n\tau)^{1/2}$ is the diffusion length of the minority carriers, and τ is the minority carrier lifetime in the CIS film. When the pump beam is turned on, the excess carriers generated in the CIS film will modulate the IR transmitted beam intensity. Under low injection conditions, the transmitted intensity of the probe beam can be expressed in terms of the unmodulated transmitted intensity (I_0), electron (n_0) and hole densities (p_0) in the absence of pump beam excitation, and the total free carrier optical absorption cross section ($\sigma_{fc} = \sigma_n + \sigma_p$), as

$$I = I_0 \exp\left[\Delta N \sigma_{fc} + \int_0^{t_f} (\sigma_n n_0 + \sigma_p p_0) dx\right], \tag{8}$$

where

$$\Delta N = \int_0^{t_f} \Delta n(x) dx. \tag{9}$$

For $\Delta I \ll I$, the fractional change in the probe beam intensity $\Delta I/I$ (with $\Delta I = I - I_0$) can be approximated as

$$\ln\left(\frac{\Delta I}{I} + 1\right) \cong \frac{\Delta I}{I} = -\sigma_{fc}\Delta N \tag{10}$$

$$= -\sigma_{fc}\left\{\frac{\alpha\phi_0(1 - R - T)\cos\theta_3}{D_n\left(\alpha^2 - \frac{1}{L_n^2}\right)}\left[L_n C_1\left(1 - e^{-\frac{t_f}{L_n}}\right) - L_f C_2\left(1 - e^{\frac{t_f}{L_n}}\right) + \frac{1}{\alpha}\left(e^{-\alpha t_f} - 1\right)\right]\right\}.$$

Assuming a highly absorbed pump beam $\left(\alpha \cong 8\times10^{4}\ \text{cm}^{-1}\right)$, and the short lifetime expected in CIS, the following simplifications are valid: (i) $\alpha L_n >> 1$, (ii) $\alpha D_n >> s_1, s_2$, (iii) $D_n^2 >> s_1 s_2 L_n^2$. Using these assumptions, equation (10) becomes:

$$\frac{\Delta I}{I} = -\sigma_{fc}\cos\theta_3\phi_0(1-R-T)\tau_{eff}\left(1-e^{-\alpha t_f}\right) \tag{11}$$

where

$$\tau_{eff} = \frac{t_f}{s_1 + t_f/\tau}, \tag{12}$$

and if $s_1 << t_f/\tau$, then $\tau_{eff} \cong \tau$.

Therefore the effective excess carrier lifetime can be calculated by substituting the measured I and ΔI into equation (11).

(2) Theory of Reflection Mode DBOM Measurement

Since CIS solar cells use thick Mo backside ohmic contacts, a modified reflection mode DBOM technique has been developed for the measurement of excess carrier lifetimes in CIS films. It is also possible to perform depth profiling of the excess carrier lifetimes in the film by changing the wavelength (and hence the absorption depth in the film) of the pump beam. Figure 2a shows a schematic diagram of the reflection mode DBOM experimental setup designed specifically for lifetime measurements in CIS films, and Figure 2b shows the incident and reflected angles of the pump beam and probe beam in the CIS device structure.

The excess electron density in the CIS layer can be obtained by solving the continuity equation, which is given by

$$\Delta n(x) = \frac{\alpha\phi_0(1-R-T)\cos\theta_3}{D_n\left(\alpha^2 - \frac{1}{L_n^2}\right)}\left(C_1 e^{\frac{x-t_f}{L_n}} + C_2 e^{\frac{-x-t_f}{-L_n}} - e^{-\alpha x}\right) \tag{13}$$

where

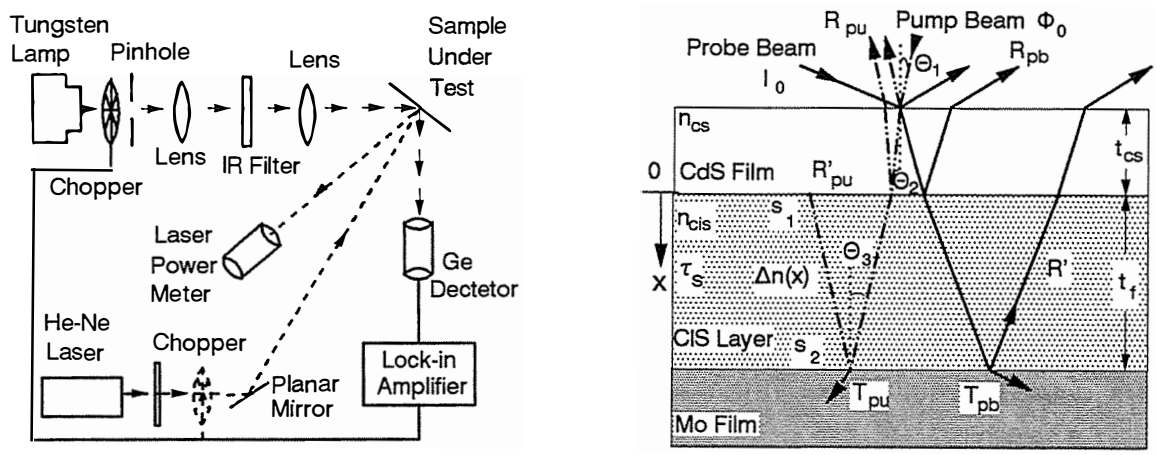

Figure 2. **(a) Schematic of reflection mode DBOM apparatus** **(b) Geometric construction used in the theory**

$$C_1 = \frac{(\alpha D_n + s_1)\left(\frac{D_n}{L_n} - s_2\right) - (\alpha D_n - s_2)\left(\frac{D_n}{L_n} + s_1\right)e^{-[t_f(\alpha - 1/L_n)]}}{2\left[\frac{D_n}{L_n}(s_1 + s_2)\cosh\left(\frac{t_f}{L_n}\right) + \left(s_1 s_2 + \frac{D_n^2}{L_n^2}\right)\sinh\left(\frac{t_f}{L_n}\right)\right]} \tag{14}$$

$$C_2 = \frac{(\alpha D_n + s_1)\left(\frac{D_n}{L_n} + s_2\right) - (\alpha D_n - s_2)\left(\frac{D_n}{L_n} - s_1\right)e^{-[t_f(\alpha - 1/L_n)]}}{2\left[\frac{D_n}{L_n}(s_1 + s_2)\cosh\left(\frac{t_f}{L_n}\right) + \left(s_1 s_2 + \frac{D_n^2}{L_n^2}\right)\sinh\left(\frac{t_f}{L_n}\right)\right]}. \tag{15}$$

Applying the charge neutrality condition for low injection, $\Delta n \cong \Delta p$, the reflected probe beam intensity can be expressed as

$$I = I_0 R' \exp\left[2\Delta N \sigma_{fc} + 2\int_0^{t_f}\left(\sigma_n n_0 + \sigma_p p_0\right)dx\right], \tag{16}$$

where

$$\Delta N = \int_0^{t_f} \Delta n(x)dx \tag{17}$$

$$= -\sigma_{fc}\left\{\frac{\alpha\phi_0(1-R-T)\cos\theta_3}{D_n\left(\alpha^2-\frac{1}{L_n^2}\right)}\left[L_nC_1\left(1-e^{-\frac{t_f}{L_n}}\right)-L_nC_2\left(1-e^{\frac{t_f}{L_n}}\right)+\frac{1}{\alpha}\left(e^{-\alpha t_f}-1\right)\right]\right\}$$

R′ is the probe beam wavelength reflectance at the CIS/Mo interface, $\sigma_{fc} = \sigma_n + \sigma_p$ is the total optical absorption cross-section of electrons and holes with $\sigma_n = 1\text{x}10^{-18}\,\lambda^2\text{cm}^2$ and $\sigma_p = 2.7\text{x}10^{-18}\,\lambda^2\text{cm}^2$ [5], and λ is the wavelength of the probe beam.

Since the absorption coefficient is very high in the CIS film for the pump beam (HeNe laser) used, and the bulk trap density in the CIS film is also high [3,6], the following conditions are valid: (i) $\alpha L_n >> 1$, (ii) $\alpha Dn >> s_1, s_2$, (iii) $D_n^2 >> s_1 s_2 L_n^2$. Based on these simplifications and the solution of equations (13) through (17), the fractional change in the probe-beam reflected intensity $\Delta I/I$ can be expressed as

$$\frac{\Delta I}{I} = -2\sigma_{fc}\cos\theta_3\phi_0(1-R-T)\tau_{eff}\left(1-e^{-\alpha t_f}\right) \tag{18}$$

where

$$\tau_{eff} = \frac{t_f}{s_1 + t_f/\tau} \tag{19}$$

is the effective excess carrier lifetime in the CIS film, which reduces to the bulk film lifetime if the front surface recombination velocity s_1 is much smaller than t_f/τ. Thus, the excess carrier lifetimes in a CIS film can be obtained by using the values of ΔI and I obtained from the DBOM measurements, and the calculated values of R and T.

(3) Experimental Aspects of DBOM Lifetime Measurement

As shown in Figures 1a and 2a, a tungsten lamp is used as the probe beam, which passes through a silicon IR filter with a cutoff wavelength $\lambda_c = 1.25\ \mu m$, and the beam is then focused to a size of about 4 mm diameter. A 1.5 mW He-Ne CW laser ($\lambda = 632.8$nm) with a beam size of about 2 mm was used as the pump beam. Both the probe beam and pump beam were chopped at 405 Hz for synchronous detection by means of a lock-in amplifier. The pump beam is reflected by using

a half-silver coated mirror which is focused onto the same spot as the probe beam on the test sample.

The experimental procedure consists of first measuring the transmitted IR intensity , I, by turning on the chopper and the tungsten lamp, and detecting the signal with the lock-in amplifier. The change in the reflected beam intensity, ΔI, was measured by superimposing the chopped pump beam onto the unchopped probe beam, and the resulting IR reflected beam intensity was measured using a lock-in amplifier. From equations (11) and (18), the excess carrier lifetime in the CIS films was calculated using the measured values of I, ΔI, and the average value of the optical and dielectric parameters listed in Table 1.

Table 1. Optical and dielectric parameters used in model.

pump beam wavelength (μm)	θ_1	absorption coefficient α (cm^{-1})	cross section σ_{fc} (cm2)	thickness of CdS film t_{cs} (μm)	thickness of CIS film t_f (μm)	index of CdS n_{cs}	index of CIS n_{cis}	index of Mo n_{mo}
0.6328	0	8.12×10^4	7.46×10^{-16}	0.08	3.4	2.5	$2.9-0.41i$	$3.6-3.5i$

Results and Discussion

(1) Validation and Exploration of DBOM Technique

(A) Test of the Model's Prediction of Linearity

To gain experience in using DBOM in transmission mode, measurements were conducted on several samples. Table 2 shows a summary of the excess carrier lifetime and the composition of these samples. The samples were provided by Brian Keyes of NREL.

Table 2. Excess carrier lifetime for 2 samples measured in transmission mode.

Samples	Composition	τ_{eff} (ns)	Measurement Mode
S670-C23S(NREL)	CIS/Glass Sub.	0.898	Transmission
S670-C14S(NREL)	CIGS/Glass Sub. (1% Ga)	0.704	Transmission

The excess carrier lifetime of the NREL CIS film was found to be longer than that of CIGS sample, in spite of the small Ga (1%) content. To validate the DBOM theory (eq. 11), different

probe beam intensities were investigated to confirm the expected linear dependence of ΔI on I (see Figures 3a and 3b). This indicates that the assumptions and approximations used in the derivation of equation 11, particularly the assumption of low level injection, apply to these experimental conditions.

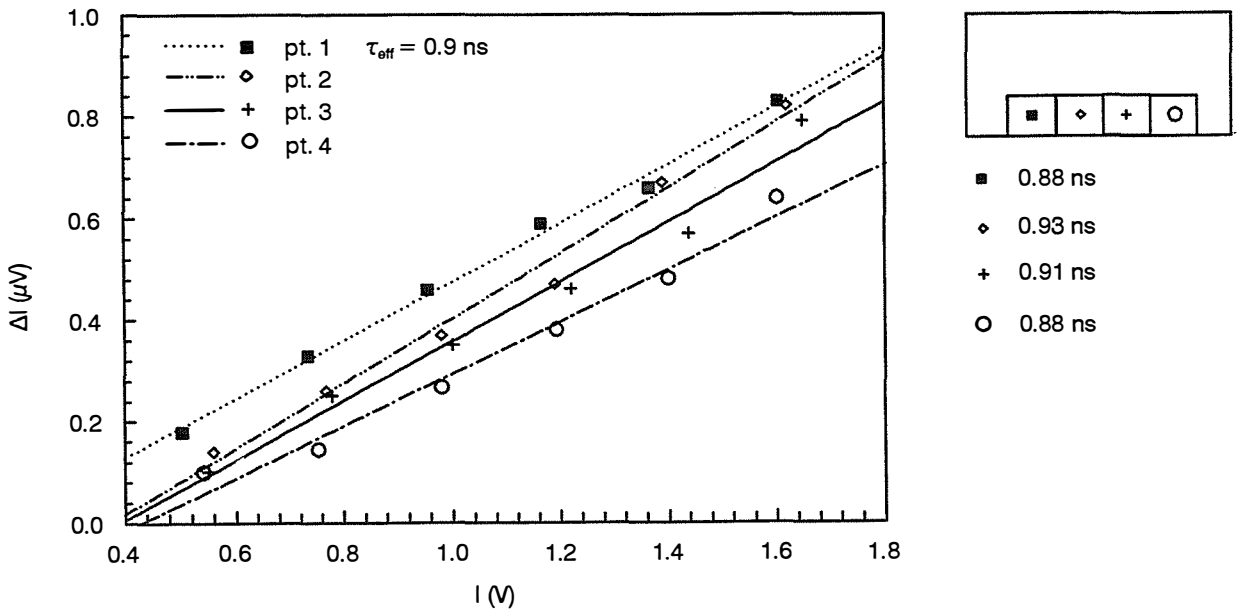

Figure 3a. The linear relationship of ΔI/I for NREL sample CIS (S670-C23S)

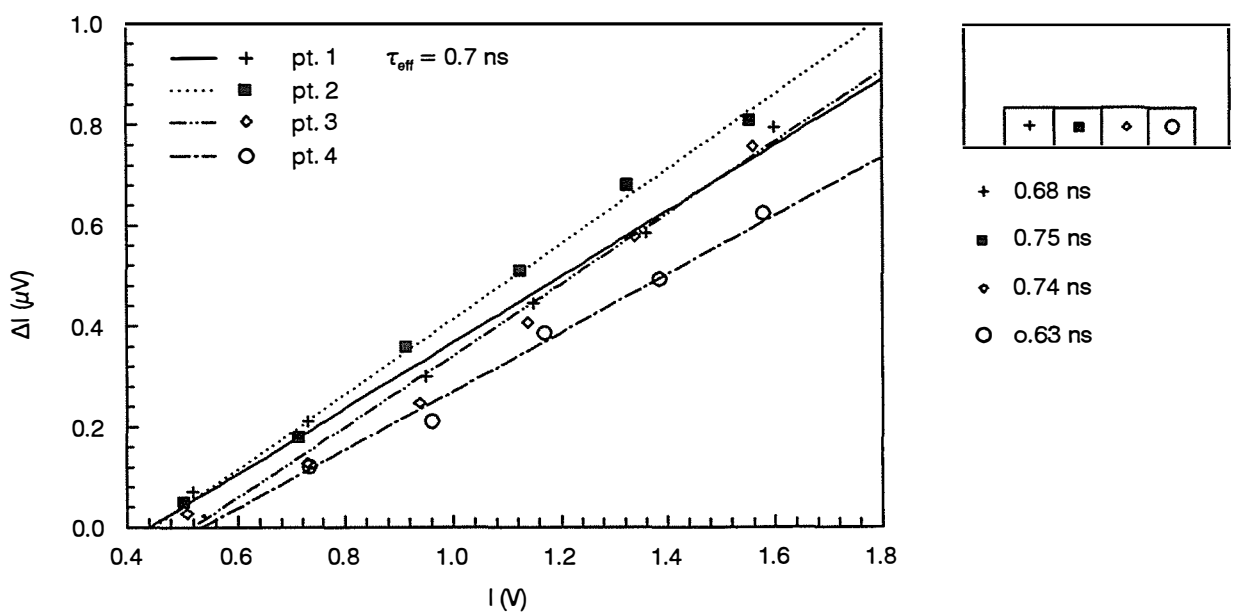

Figure 3b. The linear relationship of ΔI/I for NREL sample CIGS (S670-C14S)

(b) Demonstration of Lifetime Variations Within CIS Films

The DBOM technique's capability for revealing variations in photogenerated excess carrier lifetime within absorber films as a function of depth within the films was explored. Two approaches were studied. First, transmission mode DBOM was employed using both front and backside illumination. Since the absorption depth of the pump beam was significantly less than the film's thickness this approach selectively measured lifetimes near the front and rear film surfaces independently. Second, by using two different wavelengths whose absorption depths within the film were different, the effective generation region could be varied. He-Ne and He-Cd pump beam lasers were used to probe lifetime deeper and shallower within the films, respectively. Note that the second approach can also be used in reflection mode DBOM.

Transmission mode DBOM measurements were performed on a 2"x2" CIS sample. The sample was prepared at USF by growing a 2.5 μm thick CIS film on a 10 nm thick Mo-coated (sputtering) soda-lime glass substrate. The CIS film was deposited on the Mo-layer by a two-step process. In the first step, the precursor layers were deposited by sputtering Cu and In and evaporation of Se. In the second step, this precursor layer was annealed to a maximum temperature of 550°C in 20 Torr of Ar. The temperature profile was tuned to achieve simultaneous optimization of the bulk and surface properties.

The average excess carrier lifetime determined by the transmission mode DBOM measurements on this sample is 2.3 ns under top-side illumination and 4.5 ns under back-side illumination. A two-dimensional (2-D) mapping of the excess carrier lifetime on this CIS sample shows that τ_{eff} varies from 0.83 ns to 3.75 ns under top-side illumination and varies from 1.7 ns to 7.3 ns under back-side illumination. Estimated values of the front surface recombination velocity for this CIS sample were in the range from of mid 10^4 to low 10^5 cm/sec. The excess carrier lifetime determined under back-side illumination is twice as large as that determined under top-side illumination, indicating that the front surface recombination velocity is significantly higher than that at the bottom-side of the CIS film or that the bulk film lifetime is higher near the back contact. The same conclusion of high front-surface recombination rate is evident in the greater effective lifetime measured using the longer wavelength He-Ne laser compared to the He-Cd laser pump beam. Table 3 summarizes the measured excess carrier lifetimes on the same CIS sample under each of these experimental conditions. Figure 4 shows the linear relationship of the measured ΔI versus I plots for both the He-Ne and He-Cd lasers, which was predicted by equation (11).

Table 3. **The excess carrier lifetime of a USF CIS sample measured by transmission DBOM under front- and back-side illumination at two wavelengths.**

Illumination / Pump Beam / Lifetime	FRONT		BACK	
	RED	BLUE	RED	BLUE
MAX (ns)	3.76	3.32	7.29	6.06
MIN (ns)	0.83	0.52	1.70	1.61
AVE (ns)	2.28	2.02	4.47	3.45

* RED : He-Ne Laser (λ=0.6328μm) BLUE : He-Cd Laser (λ=0.442μm)

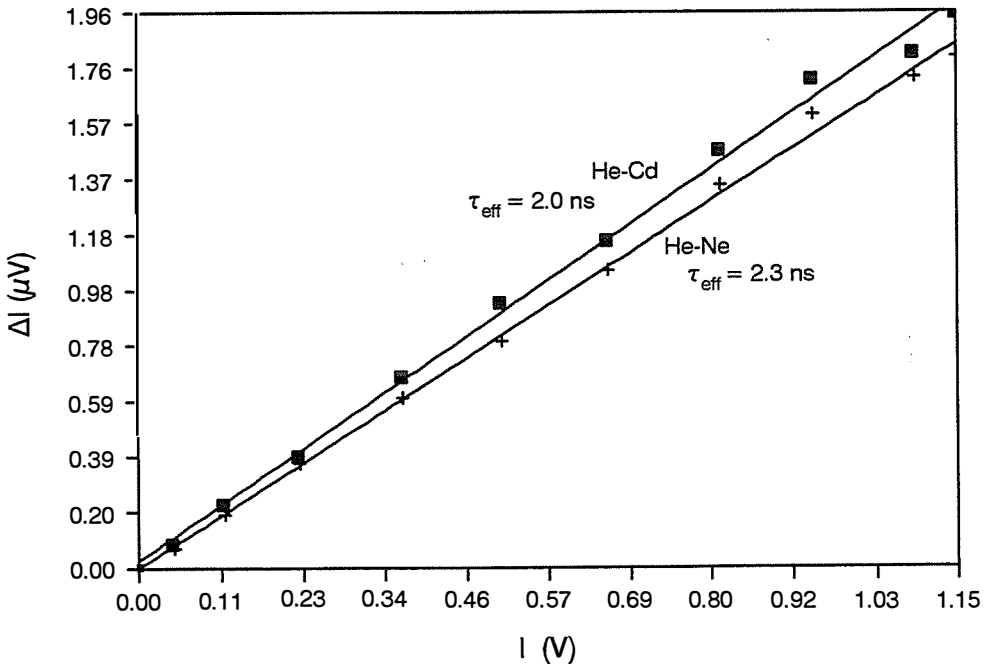

Figure 4. **The linear relationship of ΔI/I under front-side illumination for both the He-Ne and He-Cd laser**

(c) Demonstration of Lifetime Variations Across a CIS Film

An advantage of this measurement technique is the capability to measure the lifetime spatially and to relate these variations to process conditions. To demonstrate this potential, a 2" x 2" CIS sample from USF was characterized at 16 locations and the results are shown in Figure 5.

1.58	0.35	2.67	1.70
1.58	0.82	2.02	1.64
1.47	1.14	1.71	0.84
0.73	2.23	1.08	0.32

Min : 0.32
Max : 2.67
Ave : 1.37

Figure 5. Areal mapping of τ_{eff} (ns) measured by transmission mode DBOM technique (USF sample C17-2-1, CIS/Mo)

(d) Comparison of Transmission and Reflection Mode DBOM Technique

The thickness of the Mo layer in typical cell structures prevents the use of DBOM in transmission mode. For this reason a reflection mode of measurement was developed. To check for consistency between the two modes, a sample with comparable reflection and transmission coefficients was tested in both modes. The sample was a CIS film provided by USF with a thin Mo film deposited on soda-lime glass substrate. Characterization by transmission mode DBOM yielded an average excess carrier lifetime of 1.37 ns, while reflection mode DBOM gave an average value of 1.11 ns. The results are considered to be in good agreement (see table 4 below).

The discrepancy in the value of average excess carrier lifetime measured by the transmission and reflection mode DBOM can be attributed to the fact that only seven random locations were probed in the reflection mode DBOM measurements, while a mapping of the lifetime across the

entire area of the sample was performed to obtain the average value list for the measurements in the transmission mode.

Table 4. Comparison between transmission and reflection mode measured lifetimes.

USF Sample	Composition	τ_{eff} (ns)	Measurement Mode
C17-2-1	CIS/Mo/Glass Sub.	1.37	Transmission
C17-2-1	CIS/Mo/Glass Sub.	1.11	Reflection

Application to Device Structures and Processing

(a) CdTe Solar Cells

Two CdTe samples from Peter Meyer of IEC were measured by DBOM in transmission mode. The first sample, SCI 15103-G4, was deposited by Closed-Spaced Sublimation (CSS) at 550°C and then heat treated to improve its photovoltaic properties. A typical conversion efficiency for a CdTe sample prepared on soda-lime glass in this manner is 10+%. The other sample, IEC 40910.31, was deposited at 250°C and subjected to post-deposition heat treatment. Cell conversion efficiency for this process is typically 9%. The following table shows the average excess carrier lifetimes of these two samples.

Table 5. Average measured excess carrier lifetime for CdTe samples.

IEC Samples	Composition	τ_{eff} (ns)	Measurement Mode
SCI 15103-G4	CdTe/CdS/SnO_2	5.18	Transmission
IEC 40910.31	CdTe/CdS/ITO	1.87	Transmission

Since the conversion efficiency of a CdTe solar cell is directly related to recombination parameters such as the minority carrier lifetime, the measured excess carrier lifetime trends are consistent with the reported device efficiencies. Thus, measured values of the excess carrier lifetime using the transmission mode DBOM technique appear to be useful in correlating conversion efficiencies of CdTe solar cells.

(b) Buffer and Window Layers on CIS

We believe we have developed a useful technique to measure excess carrier lifetimes in a quick and nondestructive manner. This technique was then applied to study the effect of buffer and window layer films on the CIS absorber's effective lifetime. Samples were collected from different sources and DBOM measurements were performed in an attempt to identify the key processes that lead to increased cell efficiency.

As a first test three samples, provided by Dr. Don Morel of University of South Florida, were tested. This sample set consisted of CIS/Mo processed films, one with a CdS buffer layer, and one with a CdS buffer layer/ZnO/ZnO$^+$ window layer. Each sample was processed from the same precursor film. The average excess carrier lifetime for each sample as measured by the reflection mode DBOM technique is summarized in Table 6.

Table 6. Average excess carrier lifetime in CIS samples measured in reflection mode.

USF Sample	Composition	τ_{eff} (ns)	Measurement Mode
C17-2-1	CIS/Mo	1.11	Reflection
	CdS/CIS/Mo	6.31	Reflection
	ZnO/ZnO$^+$/CdS/CIS/ Mo	16.40	Reflection

The results show that the CdS buffer layer has a significant effect on the observed excess carrier lifetime in the CIS film. The value of average excess carrier lifetime for the CIS sample with the CdS layer is nearly 6 times higher than that of the sample without the CdS layer. The ZnO/ZnO$^+$ also significantly contributes to improving the measured excess carrier lifetime. The value of average excess carrier lifetime for the sample with ZnO/ZnO$^+$/CdS structure is about 16 times higher than that of the bare CIS film.

Another set of samples was provided by Dr. Shafarman, IEC, University of Delaware, in which Ga was added (CIGS). These $CuInGaSe_2$ samples with different Ga contents were deposited on 1"x1" soda-lime glass with a 1 μm thick sputtered Mo layer. The measured excess carrier lifetime, composition, and energy band gap are summarized in the following table.

Table 7. Average excess carrier lifetime in CIGS samples measured in reflection mode.

IEC Samples	Composition	Ga %	E_g (ev)	τ_{eff} (ns)	Measurement Mode
32588.12	CIGS/Mo	11.2	1.28	0.81	Reflection
32518.21	CIGS/Mo	14.6	1.36	0.51	Reflection
32618.12	CdS/CIGS/Mo	14.6	1.36	1.36	Reflection

It is evident that the sample with the CdS buffer layer showed a higher excess carrier lifetime than the two samples without the buffer layer. Based on the information provided by Bill Shafarman [7], the first sample, with energy band gap less than 1.3 eV, produced a device with a 15% total area efficiency; a value which is higher than the other two samples. The DBOM results are consistent with a positive correlation between lifetime and efficiency and support a significant positive influence of the CdS buffer layer on CIGS.

(c) Buffer Layer Processing

To better understand the role of CBD CdS deposition on the excess carrier lifetime, a set of experiments was performed as outlined in Figure 6. Four nominally identical CIGS precursor films were obtained from NREL and the lifetime was measured on each as-received film. A CdS sulfide buffer layer was then deposited on each sample using 4 different processes. In these experimental designs, MOCVD was used to isolate the effect of the electrolyte composition used in CBD.

CIGS films grown at NREL on Mo coated soda-lime glass substrates were used in this study. Devices fabricated at NREL using their standard CBD CdS/ZnO processes on other portions of the same substrates used in this study (Figure 3) yielded uniform efficiencies of about 15% with a V_{oc} spread of 0.576V to 0.584V, and FF from 74.5% to 75.44% (seven devices measured). EPMA data taken along a 2"x(1/8)" strip showed a gradient in the elemental compositions from one side of the samples to the other. The Cu varied from 20.3% to 21.24%, In from 21.2% to 20.7%, Ga from 6.95% to 7.09%, and Se from 51.5% to 50.9% (10 points measured). The samples used for the partial electrolyte studied were not fabricated into devices but are believed to be comparable to similar samples with efficiencies of about 14%. EMPA data taken on these substrates showed elemental abundances of Cu 23.72% (± 0.123%), In 18.76 (± 0.11%), Ga 7.2% (± 0.06%), and Se 50.3% (± 0.09%). These substrates were further divided and ESCA

measurements of the surface and near-surface composition profiles taken. The ESCA data showed that the surfaces of all these films were significantly enriched with indium compared to their average compositions in the copper-depleted near-surface region.

Figure 6 schematically illustrates the four processing conditions studied and measurements conducted in each case. The baseline CBD solution consisted of NH_3 (1.44×10^{-4}M), NH_4Cl (7.43×10^{-4}M), $CdCl_2$ (2.4×10^{-4}M), and NH_2CSNH_2 (2.4×10^{-3}M). The cadmium partial electrolyte consisted of a solution with the same reactants except the thiourea was absent and the sulfur partial electrolyte contained the baseline reactants in the same concentration except the cadmium salt was absent. The aqueous processing was conducted at a bath temperature of 80 to 85°C with continuous stirring. Processing times for the partial electrolyte cases are identical to the baseline CBD process, which produced a uniform, compact, coherent, and colloid-free film with a thickness of about 80 nm. MOCVD growth of CdS was performed in a horizontal, atmospheric pressure, cold wall reactor using dimethyl cadmium and hydrogen sulfide reactants in hydrogen at a substrate temperature of 160±10°C and a VI/II reactant ratio of 100/1 for 2.8 min. The MOCVD growths were exposed for approximately 1 minute to H_2S before the flow of dimethyl cadmium was initiated. DBOM measurements were conducted on sixteen distinct points on each substrate at each step in the process (see Figure 6).

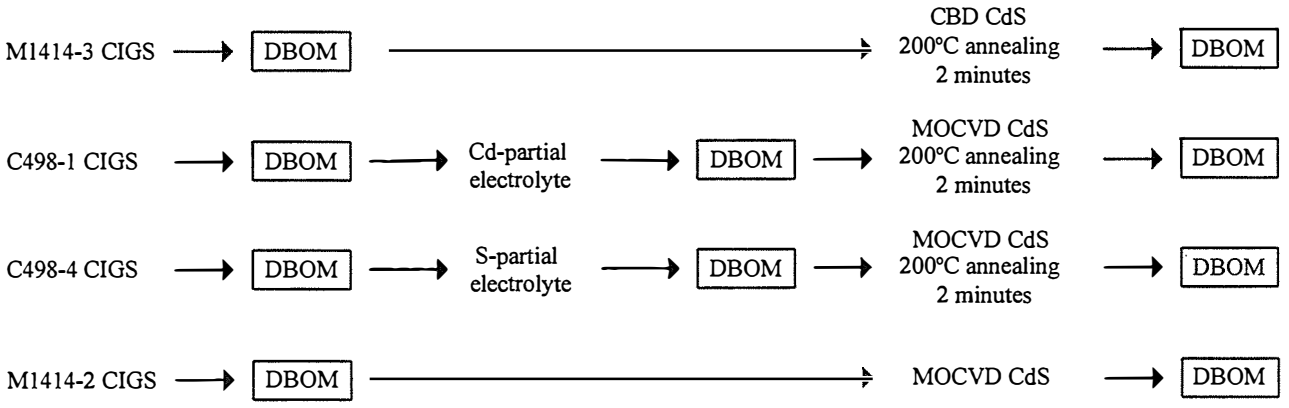

Figure 6. Processing sequence for the 4 NREL CIGS samples

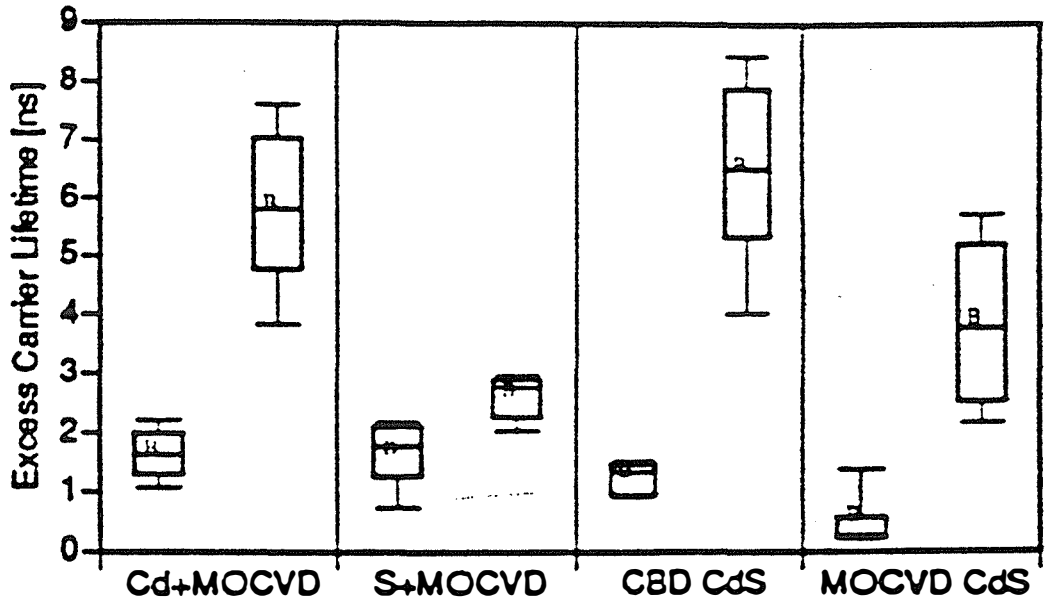

Figure 7. Box plot of lifetime data statistical summary from buffer layer processing

Figure 7 is a Box plot showing the statistical summary of the excess carrier lifetime data taken for each processing sequence. It is observed that the initial lifetime values for the films (< 3 ns) are typically improved by a factor of 2 to 3 in each case except the aqueous sulfur electrolyte exposure. This result is strong negative evidence for attributing the beneficial effects on CIGS device performance of the CBD CdS process to sulfur passivation, an effect well established in the case of III-V compound semiconductors. Furthermore, the data do not support the alternative hypothesis that cadmium ion reactions with the surface during the CBD process alone are responsible for the dramatic lifetime improvement. This is concluded from the results with the cadmium partial electrolyte case subsequent to the MOCVD growth of CdS. The lifetime measured immediately after aqueous processing showed no significant change compared to their initial value. Indeed, considering the substantially poorer initial lifetime in the MOCVD control sample compared to the CBD control and cadmium partial electrolyte samples, it appears that the beneficial effect these treatments confer on lifetime is provided equally well by the MOCVD growth process alone. Since all the samples were baked in air before final measurement except the MOCVD control sample, the possibilities that oxidation or higher temperature interdiffusion effects are required to achieve high lifetimes are not supported by this data. Since the MOCVD control (which was not subjected to any aqueous processing) had a beneficial effect, and the

aqueous sulfur electrolyte exposure a neutral effect, water exposure alone cannot be responsible for the observed lifetime increases.

Figures 8 and 9 show four sets of DBOM data of the spatial inhomogeneity in excess carrier lifetimes exhibited in these very high quality films. Future studies will utilize this capability in conjunction with materials characterization to seek correlation with material parameters and defect structures which control recombination processes in these device structures.

SUMMARY

In summary we have applied transmission mode DBOM to CdTe devices and CIS test structures. We have also demonstrated a contactless reflection mode DBOM technique developed specifically for measuring the excess carrier lifetimes in CIS films. A study of the effects of CBD and MOCVD deposited CdS on excess carrier lifetimes in CIGS films has been conducted. We have shown that both the CBD and MOCVD processes for CdS buffer layer formation significantly increase the effective excess carrier lifetimes of CIGS films with respect to their as-grown values. We believe these results firmly exclude several hypotheses proposed to explain the beneficial effects of the CBD CdS process but do not yet enable us to unequivocally explain the underlying mechanism. Further study of the correlation between the excess carrier lifetimes, material characteristics and defect structures in CIGS films, and the performance parameters of CIGS solar cells, is needed to optimize the conversion efficiency of thin film CIS-based solar cells.

References

[1] J.R. Tuttle, J.S. Ward, A. Duda, T.A. Berens, M.A. Contreras, K.R. Ramanathan, A.L. Tennant, J. Keane, E.D. Cole, K. Emery, and R. Noufi, *Proceedings of the 1996 Spring MRS Meeting*, San Francisco, CA, 8-12 April, 1996 (in press).

[2] T.R. Hanak, A.M. Bakry, D.J. Dunlavy, F.A. Elfotouh, R.K. Ahrenkiel and M.L. Timmons, "Deep-level Transient Spectroscopy of AlGaAs and $CuInSe_2$," *Solar Cells,* **27**, pp. 347-356, 1989.

[3] R.K. Ahrenkiel, "Photocapacitence of CdZnS/$CuInSe_2$ Thin-film Heterojunctions," *J. Appl. Phys.*, **59**(1), 1986.

[4] Y.S. Chang, Sheng S. Li, "Measurements of Silicon Film and Buried Oxide Thickness in SOI Wafers by a Contactless S-polarized Reflectance Technique," *6th Int. Symp. on SOI Tech. and Devices*, pp. 513, 1994.

INITAL

C498-1

1.16	1.17	0.88	0.86
1.54	1.45	1.59	1.17
1.85	1.79	1.68	1.57
2.25	2.20	2.14	2.17

Min : 0.86
Max : 2.25
Ave : 1.59

ESCA

C498-4

1.87	2.18	2.24	1.95
2.41	2.18	2.02	1.60
2.27	2.00	1.61	0.88
1.79	1.62	0.93	0.41

Min : 0.41
Max : 2.41
Ave : 1.75

After MOCVD CdS

C498-1 Cd-partial electrolyte

6.01	7.80	7.53	8.81
5.01	6.88	6.63	10.31
3.87	5.61	7.17	7.83
3.72	4.59	4.93	6.09

Min : 3.72
Max : 10.31
Ave : 6.20

ESCA

C498-4 S-partial electrolyte

1.55	1.96	2.06	2.40
1.87	2.13	2.75	2.70
2.59	2.77	2.90	3.00
2.85	2.98	2.87	2.90

Min : 1.55
Max : 3.00
Ave : 2.52

Figure 8. **The spatial distribution of the excess carrier lifetime τ_{eff} (ns) for NREL CIGS samples C498-1 and C498-4**

INITAL

M1414-3 M1414-2

1.26	0.97	1.11	0.88	ESCA	1.63	1.62	1.29	0.84
1.47	1.44	1.45	1.52		0.98	0.66	0.42	0.26
1.58	1.54	1.47	1.56		0.50	0.23	0.18	0.20
0.87	0.94	0.93	0.66		0.41	0.32	0.26	0.24

Min : 0.66
Max : 1.58
Ave : 1.23

Min : 0.18
Max : 1.63
Ave : 0.60

FINAL

M1414-3 CBD CdS M1414-2 MOCVD CdS

6.75	9.36	7.90	6.49	ESCA	4.06	2.72	2.31	2.15
6.80	8.06	7.89	6.58		5.29	4.29	2.84	2.14
5.24	6.26	5.97	5.32		7.47	6.01	5.09	3.23
4.01	5.42	4.02	3.60		9.46	5.56	5.28	4.35

Min : 3.60
Max : 9.36
Ave : 6.23

Min : 2.14
Max : 9.46
Ave : 4.53

Figure 9. The spatial distribution of the excess carrier lifetime τ_{eff} (ns) for NREL CIGS samples M1414-2 and M1414-3

[5] D.K. Schroder, R.N. Thomas and J.C. Swartz, "Free Carrier Absorption in Silicon," *IEEE Trans. Electron Devices*, **ED-25**, pp. 254-261, 1978.

[6] C. Goradia and M. Ghalla Coradia, "Theory of High Efficient (Cd,Zn)S/$CuInSe_2$ Thin Film Solar Cell," *Solar Cells*, **16**, pp. 611-630, 1986.

[7] W.N. Shafarman, R. Klenk and B.E. McCandless, "Characterization of $Cu(InGa)Se_2$ Solar Cells with High Ga Content," *Conference Record of the 25th IEEE PVSC*, 1996.

THERMODYNAMIC ASSESSMENT OF THE Cu-In-Se SYSTEM

Introduction

Although considerable progress has been achieved in CIS-based PV processing technology, the chemical and phase complexity of this materials system has limited process optimization efforts and our detailed understanding of process mechanisms. As an example, it would be useful if the shape of the ternary liquidus surface and the eutectic valley, along with the equilibrium vapor composition, were known. This knowledge could suggest precursor film structures and elemental deposition fluxes that could lead to lower a $CuInSe_2$ formation temperature and more rapid growth kinetics (e.g., liquid phase assisted). There are also questions concerning junction formation, substitutional incorporation of Ga for In and its relation to processing, and the interactions of CIS with the buffer layer materials. A starting point to understanding the reaction pathways in CIS processing is to establish the phase equilibria in this materials system. Thus a portion of our effort has been devoted to a systematic assessment of the thermochemistry and phase equilibria in the Cu-In-Se system.

Performing a critical assessment of a multicomponent system begins with an examination of the unary systems and proceeds sequentially to the higher order ones. Standard CALPHAD (CALculation of PHAse Diagrams) procedures were used in the critical evaluation, including application of the Lukas [1] and ThermoCalc [2] software systems. Our review of the recent literature concluded that acceptable assessments are available only for the Cu and In unary systems and the Cu-In binary system. During the first year of work, a full assessment of the Se unary system was performed and preliminary assessments of the In-Se and Cu-Se binaries were completed. The results of this effort are outlined below.

Se System

The stable solid phase of selenium exhibits a hexagonal structure and melts at 494.3 K. The liquid phase of pure selenium is complex due to vibrational energy contributions, free volume effects, and both ring-chain and depolymerization reactions. Like sulfur, selenium exhibits a complex structure in the vapor phase. Mass-spectrometric measurements have shown the presence of each of the molecular species ranging from the monomer to Se_{10}; the more abundant species being Se_2 through Se_8. Studies of the molecular composition of selenium vapor have been performed using a variety of methods. These include vapor density, optical absorption, torsion and Knudsen effusion measurements, and mass-spectrometry.

The assessment of the thermodynamic properties of Se(c, hexagonal), Se(ℓ) and Se_n(g){n = 1 to 8} resulted in suggested values of $\Delta H^\circ_{f,298}$, S°_{298}, and $C_p(T)$. The thermodynamic functions of the gaseous phase were assessed from literature data or calculated from molecular constants assuming harmonic oscillator, rigid rotor, and ideal gas behavior. Second and third law analyses were performed on literature data to evaluate a value of $\Delta H^\circ_{f,298}$ for Se_n(g). The values of $\Delta H^\circ_{f,298}$ for Se_5(g) and Se_6(g) were optimized using the vapor pressure data measured above Se(ℓ) and Se(c,hexagonal), respectively. Gas phase nonidealities were taken into account by using the Peng-Robinson equation of state. Figures 10 and 11 show the calculated total pressure above solid and liquid Se. Also shown in these figures are the reported experimental values, and these data compare very well with the assessed total pressure.

The results of this assessment are expressions for the Gibbs energy of each of the ten species Se(c,hexagonal), Se(ℓ) and Se_n(g) {n = 1-8} as a function of temperature (Table 8). These expressions were then used to calculate equilibria in the Se system. In Figures 12 and 13 the calculated gas phase compositions above solid and liquid Se are shown.

It is interesting to note that the predominant vapor species at a temperature above approximately 1000 K is the dimer, while at a lower temperature (~ 600 to 1000 K), Se_5(g) is the dominant species. Below 600 K the major species is Se_6(g). During growth using a Se evaporation source, a change in deposition chemistry might be expected as the temperature is changed through one of these transitions.

The results of our Se assessment were used to estimate the Langmuir evaporation flux that is useful in characterizing the performance of an evaporative source. The Hertz-Langmuir equation

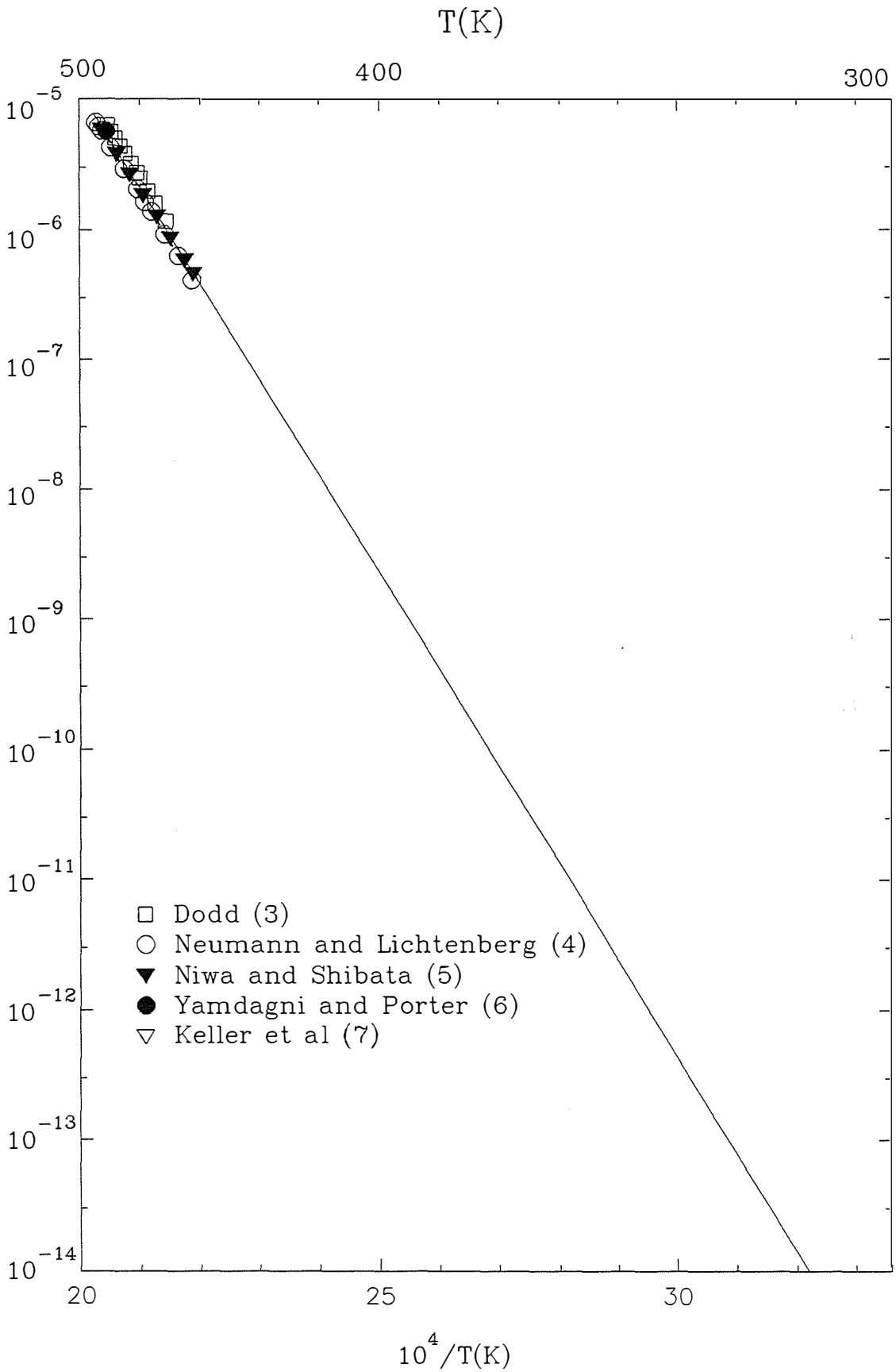

Figure 10. Comparison between experimental and assessed total pressure over solid Se from 298 to 494 K

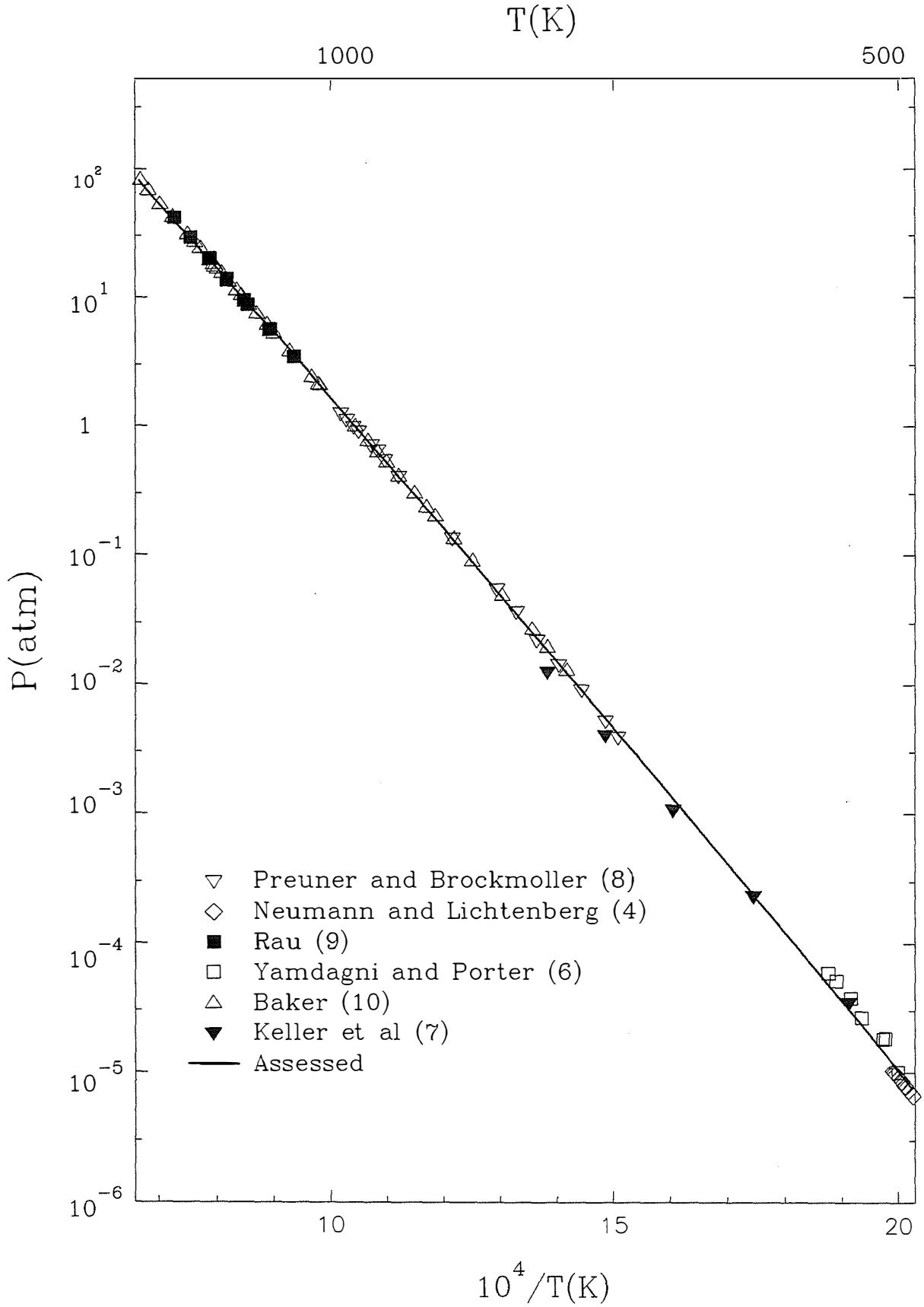

Figure 11. Comparison between the experimental and assessed total pressure over liquid Se from 494 to 1500 K

Table 8. Optimized values of the Gibbs energy relative to H_{SER} of Se species. The gas phase Se species are at a standard vapor pressure of 1 atm.

Phase	Temperature Range (K)	$G-H_{SER}$(J/K.mol)
Solid Se (hexagonal)	298.15 to 494.3	$-6.657\times10^{3} + 92.540T - 19.14\,T\ell nT - 1.2295\times10^{-2}\,T^{2} + 2.677\times10^{-6}\,T^{3}$
Solid Se (metastable)	494.3 to 760*	$-6.657\times10^{3} + 92.540T - 19.14\,T\ell nT - 1.2295\times10^{-2}\,T^{2} + 2.677\times10^{-5}\,T^{3}$
Solid Se (metastable)	760 to 1200*	$-9.0592\times10^{3} + 150.33T - 28.552\,T\ell nT$
Liquid Se (supercooled)	298.15 to 494.3**	$-9.8092\times10^{3} + 288.81T - 52.4\,T\ell nT + 2.4925\times10^{-2}\,T2 - 5.455\times10^{-6}\,T^{3}$
Liquid Se	494.4 to 1000	$-9.8092\times10^{3} + 288.81T - 52.4\,T\ell nT + 2.4925\times10^{-2}\,T2 - 5.455\times10^{-6}\,T^{3}$
Liquid Se	1000 to 1150	$8.4331\times10^{3} - 78.47T + 5.399\,T\ell nT - 3.5945\times10^{-2}\,T^{2} - 5.202\times10^{-6}\,T^{3}$
Liquid Se	1150 to 1500	$-7.4606\times10^{3} + 192.65T - 36\,T\ell nT$
Se(g)	298.15 to 600	$2.3184\times10^{5} - 45.308T - 19.56\,T\ell nT + 6.635\times10^{-4}\,T^{2} - 0.6452\times10^{-6}\,T^{3} - 2.3130\times10^{4}/T$
Se(g)	600 to 2000	$2.2848\times10^{5} - 17.544T - 23.23\,T\ell nT - 9.015\times10^{-4}\,T^{2} + 0.1326\times10^{-6}\,T^{3} + 3.9835\times10^{5}/T$
Se_2(g)	298.15 to 600	$1.2739\times10^{5} + 125.16T - 57.0\,T\ell nT + 2.184\times10^{-2}\,T^{2} - 4.797\times10^{-6}\,T^{3} + 2.1470\times10^{5}/T$
Se_2(g)	600 to 2000	$1.3739\times10^{5} - 22.761T - 34.14\,T\ell nT - 2.1355\times10^{-3}\,T2 + 8.142\times10^{-8}\,T^{3} - 6.255\times10^{5}/T$
Se_3(g)	298.15 to 2000	$1.6348\times10^{5} - 75.763T - 58.006\,T\ell nT - 1.1105\times10^{-4}\,T^{2} + 1.114\times10^{-8}\,T^{3} + 9.830\times10^{4}/T$
Se_4(g)	298.15 to 2000	$1.4083\times10^{5} + 212.95T - 82.578\,T\ell nT - 3.2385\times10^{-4}\,T^{2} + 3.250\times10^{-8}\,T^{3} + 2.6765\times10^{5}/T$
Se_5(g)	298.15 to 2000	$1.1988\times10^{5} + 309.11T - 107.77\,T\ell nT - 1.834\times10^{-4}\,T^{2} + 1.843\times10^{-8}\,T^{3} + 2.4385\times10^{5}/T$
Se_6(g)	298.15 to 2000	$9.9732\times10^{4} + 453.60T - 132.73\,T\ell nT - 1.7125\times10^{-4}\,T^{2} + 1.722\times10^{-8}\,T^{3} + 2.8925\times10^{4}/T$
Se_7(g)	298.15 to 2000	$1.0046\times10^{5} + 453.60T - 132.73\,T\ell nT - 2.202\times10^{-4}\,T^{2} + 2.213\times10^{-8}\,T^{3} + 3.541\times10^{5}/T$
Se_8(g)	298.15 to 2000	$1.0096\times10^{5} + 694.55T - 182.49\,T\ell nT - 2.4180\times10^{-4}\,T^{2} + 2.432\times10^{-8}\,T^{3} + 3.9225\times10^{5}/T$

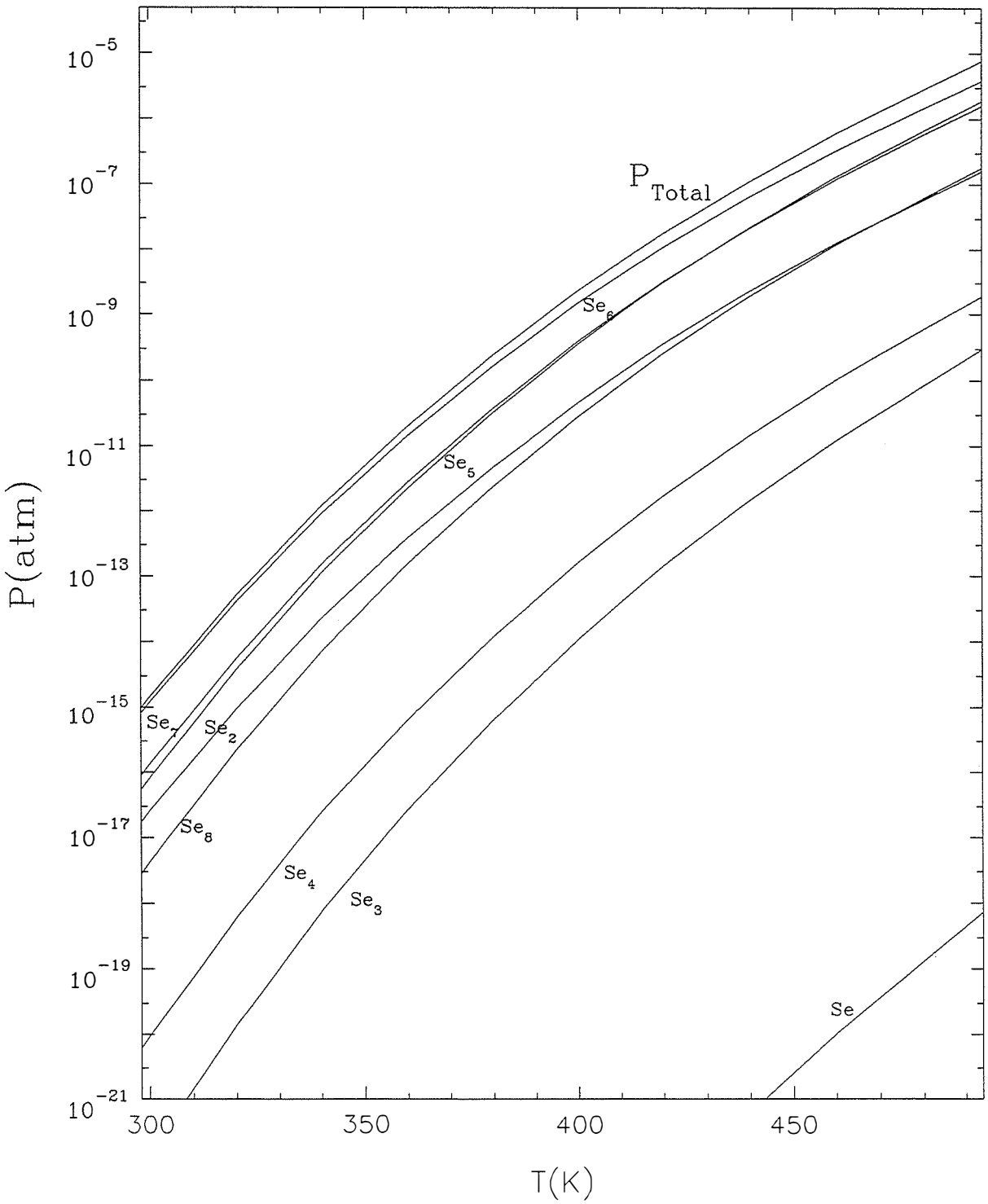

Figure 12. Assessed total and partial pressures over solid Se from 298 to 494 K

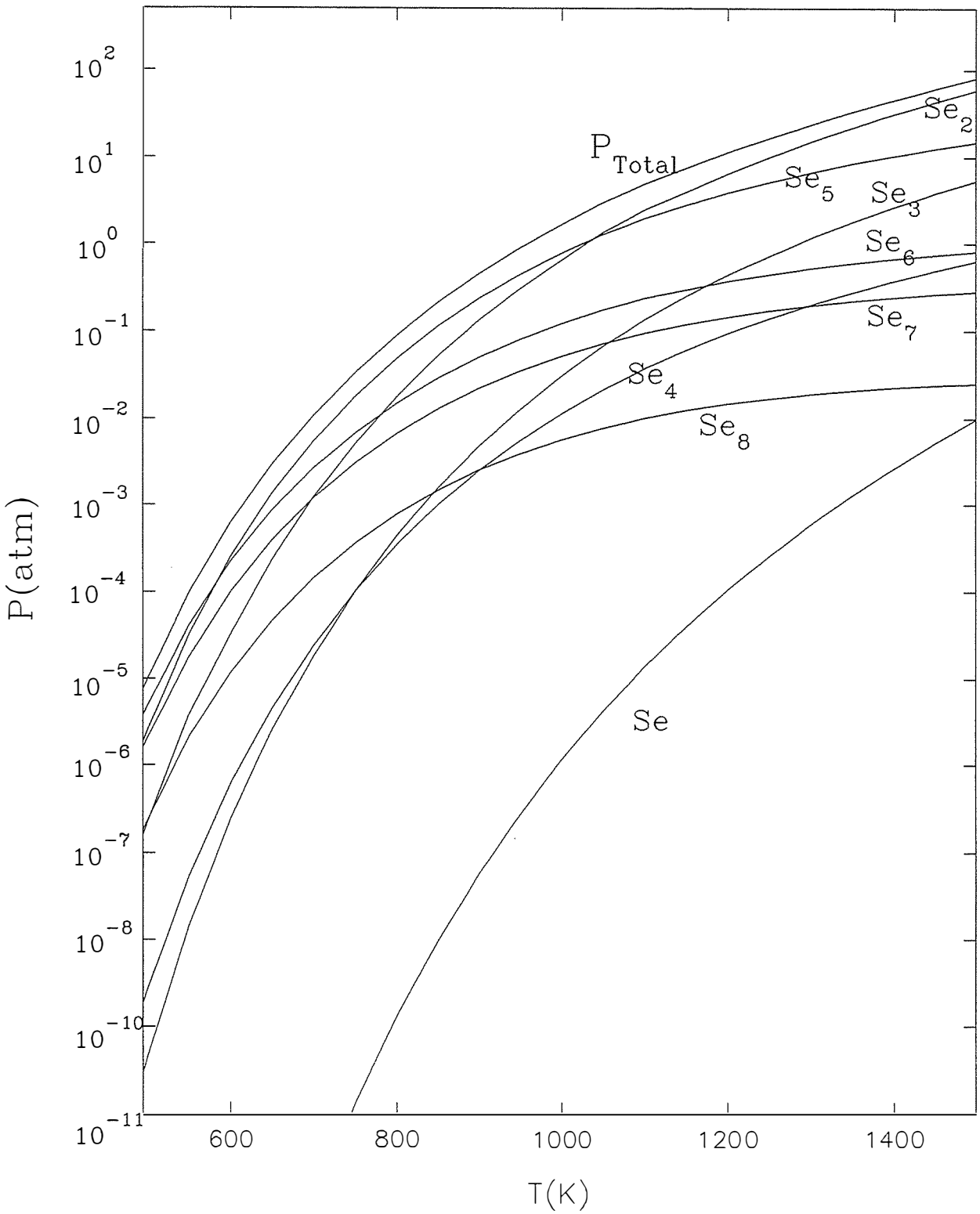

Figure 13. Assessed total and partial pressures over liquid Se from 494 to 1500 K

$$J_{Se_n} = \alpha N_A P_{Se_n} / \sqrt{2\pi M_{Se_n} RT} \quad (1)$$

was used, where

α	=	evaporation coefficient
N_A	=	Avogadro's number
P_{Se_n}	=	partial pressure of $Se_n(g)$
M_{Se_n}	=	molecular weight of $Se_n(g)$

The evaporation coefficients for $Se_n(g)$ were studied by Huang et al. [11], and the data were assessed by Drowart et al. [12]. They determined that $\alpha = 0.23$ for each of the $Se_n(g)$ species, a result adopted for this calculation as well as the assumption that the temperature dependence of α is negligible. The results are given in Fig. 14.

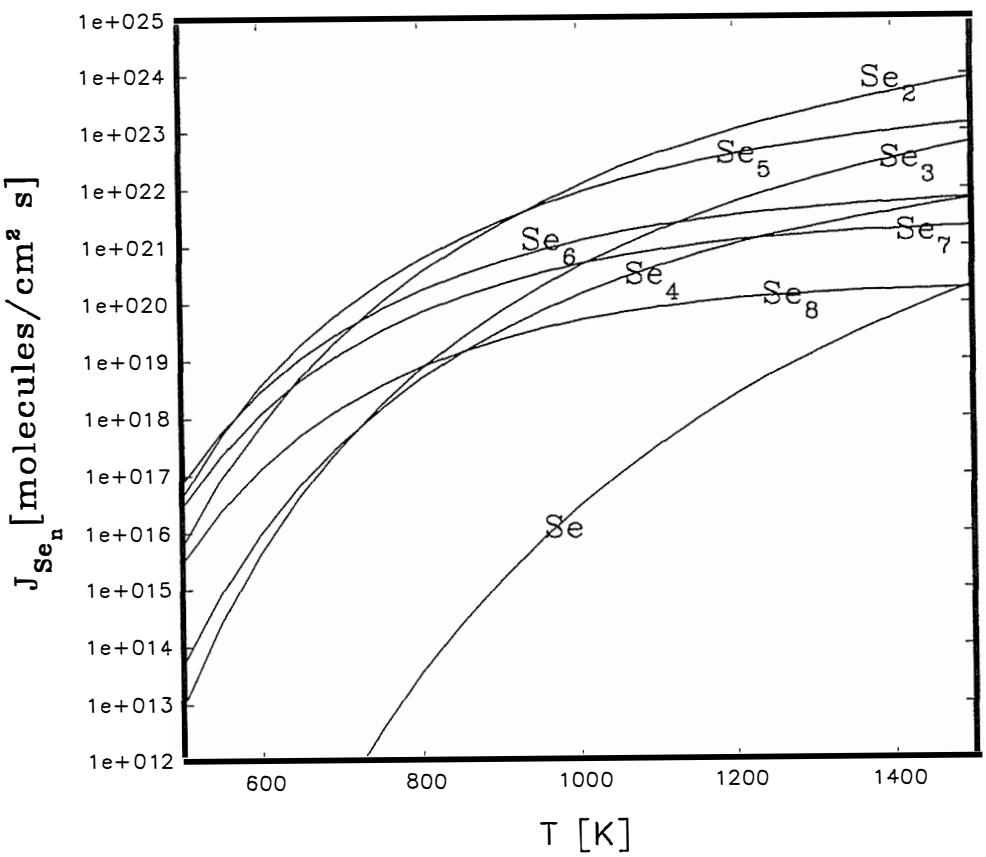

Figure 14. The calculated free evaporative $Se_n(g)$ flux above liquid selenium

In-Se Binary System

(1) Assessment

The phase diagram and thermochemistry of the In-Se system has been experimentally studied by several authors and the results for selected properties are inconsistent. Early studies [13] performed by DTA and X-ray analyses reported four intermediate compounds (In_2Se, InSe, In_5Se_6 and In_2Se_3), while InSe and In_2Se_3 were identified as congruent melting compounds. A miscibility gap on the In-rich side of the phase diagram was also suggested. Later work [14,15] reported the existence of the four compounds In_4Se_3 (instead of In_2Se), InSe, In_6Se_7 (instead of In_5Se_6), and In_2Se_3, with only the In_2Se_3 melting congruently. In addition, liquid-liquid miscibility gaps on both sides of the phase diagram were observed. Experimental measurements of $\Delta H^{\circ}_{f,298}$ are available for each compound. Both low and high temperature heat capacity measurements have been reported for each compound with the exception of In_4Se_3.

The complete database for In-Se system was assembled and selected data analyzed in view of changes in compound stoichiometry and the Se vapor thermodynamic properties. The selected database was combined with the unary data for indium provided by SGTE [16] and the assessed Se data previously discussed. The resulting experimental data were assigned uncertainties and then optimized using the BINGSS routine [1]. In this procedure, the parameters describing the temperature dependence of the Gibbs energy of the liquid solution were optimized using a maximum likelihood algorithm.

The phase stability expressions for the pure indium and selenium are given relative to the Standard Element Reference (SER) as follows,

$$G - H_{SER} = A + BT + CT\ln T + DT^2 + ET^3 + F/T + GT^7 + HT^{-9} \qquad (2)$$

Each compound in the In-Se system was treated as a stoichiometric compound with a temperature dependence of the Gibbs energy as follows,

$$G - H_{SER} = A + BT + CT\ln T + DT^2 + ET^3 + F/T \qquad (3)$$

The Redlich-Kister polynomial expression for the Gibbs energy of the liquid phase has the form,

$$G - H^{SER} = \left({}^0G_{In} - {}^0H_{In}^{SER}\right)x_{In} + \left({}^0G_{Se} - {}^0H_{Se}^{SER}\right)x_{Se}$$
$$+RT\left(x_{In}\ell n x_{In} + x_{Se}\ell n x_{Se}\right) + x_{In}x_{Se}\sum_{v=0}^{n} K_v\left(x_{In} - x_{Se}\right)^v \tag{4}$$

where the K_v are functions of temperature, fitted to

$$K_v = a_v + b_v T + c_v T \ln T + \cdots \tag{5}$$

The first two terms in Equation (4) represent the contribution of the pure elements to the Gibbs energy of the mixture, while the third term represents the ideal entropy of mixing contribution and the last term is the excess Gibbs energy of mixing.

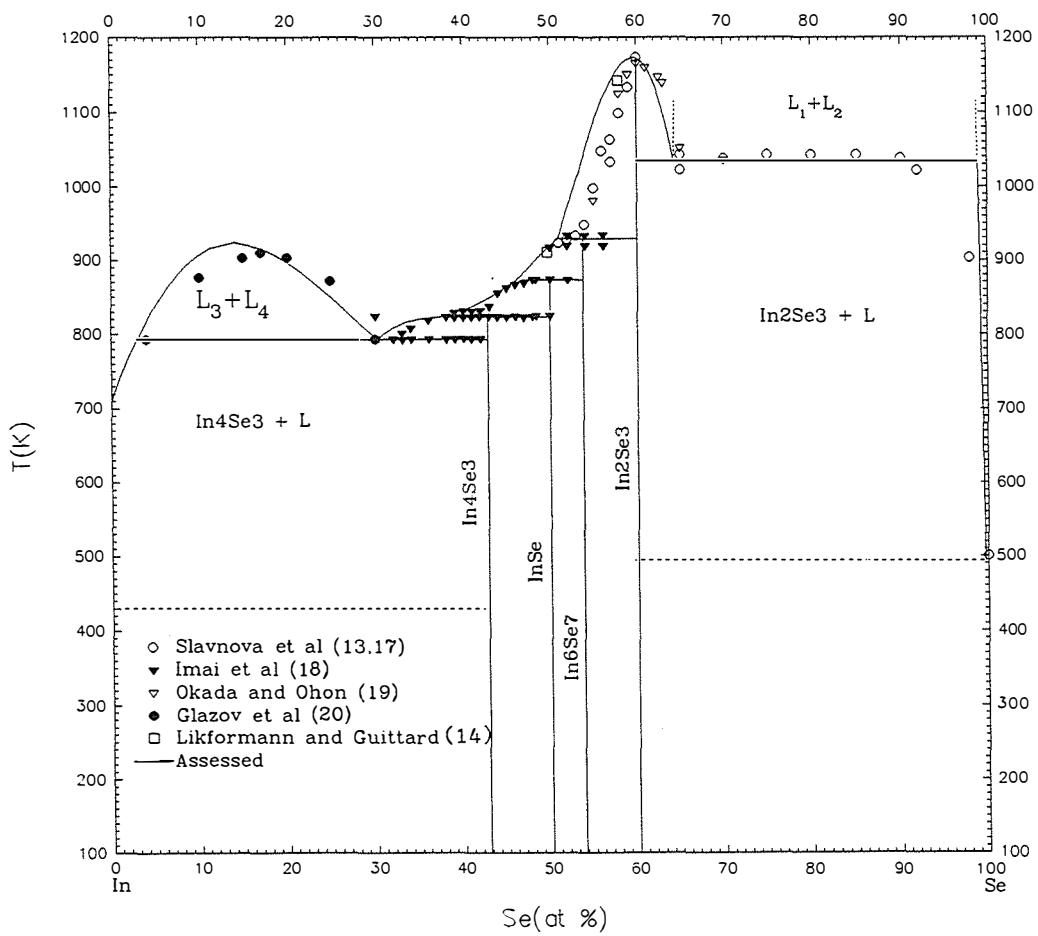

Figure 15. Assessed In-Se temperature-composition phase diagram

An assessment of the In-Se system was performed using these models to describe each phase. Good agreement with the selected experimental data was found. Figure 15 shows the assessed phase diagram (solid/dashed lines) and compares the calculated phase diagram to the experimental measurements. Four line compounds were included with only In_2Se_3 melting in a congruent fashion.

Table 9. Optimized Gibbs energy expressions for compounds in the In-Se system.

Compound	Temperature range (K)	$G-H_{SER}$ (J/K mol)
In_2Se_3	298.15 to 486	$-3.1017\times10^5 + 5.7423\times10^2\,T - 1.1192\times10^2\,T\ell nT - 2.0645\times10^{-2}\,T^2$
	486 to 623	$-3.0717\times10^5 + 5.9549\times10^2\,T - 1.1687\times10^2\,T\ell nT - 1.406\times10^{-2}\,T^2$
	623 to 1023	$-2.9732\times10^5 + 4.8652\times10^2\,T - 1.0111\times10^2\,T\ell nT - 1.406\times10^{-2}\,T^2$
	1023 to 1072.58	$-3.1639\times10^5 + 8.7150\times10^2\,T - 1.58\times10^2\,T\ell nT$
In_6Se_7	298.15 to 928.78	$-7.9960\times10^5 + 1.8077\times10^3\,T - 3.4757\times10^2\,T\ell nT + 3.3415\times10^{-2}\,T^2$
InSe	298.15 to 873.16	$-1.1010\times10^5 + 2.6075\times10^2\,T - 52.32\,TT\ell nT + 3.14\times10^{-3}\,T^2$
In_4Se_3	298.15 to 823.26	$-3.7536\times10^5 + 1.0411\times10^2\,T - 1.9663\times10^2\,T\ell nT - 1.2118\times10^{-2}\,T^2 + 1.4644\times10^6/T$

The optimized Gibbs energy formulas for the intermediate compounds are given in Table 9. With these expressions for the Gibbs energies of the compounds as well as those for the condensed solution and gas phase molecular species, it is possible to calculate various equilibrium situations. As an example, Figures 16 and 17 shows the equilibrium Se_2, In and In_2Se partial pressures above solid In_2Se_3 as a function of reciprocal temperature. A comparison of the vapor pressures at a temperature of 1072.58 K, the maximum and melting temperature of In_2Se_3, indicates that the Se_2 pressure is significantly greater than the In or In_2Se partial pressures. Thus solid In_2Se_3 is expected to vaporize incongruently to yield an In-rich liquid in equilibrium with $In_2Se_3(s)$ at elevated temperature. These vapor pressure curves are double valued at a given temperature, corresponding to equilibrium between $In_2Se_3(s)$ and either Se-rich or In-rich phases.

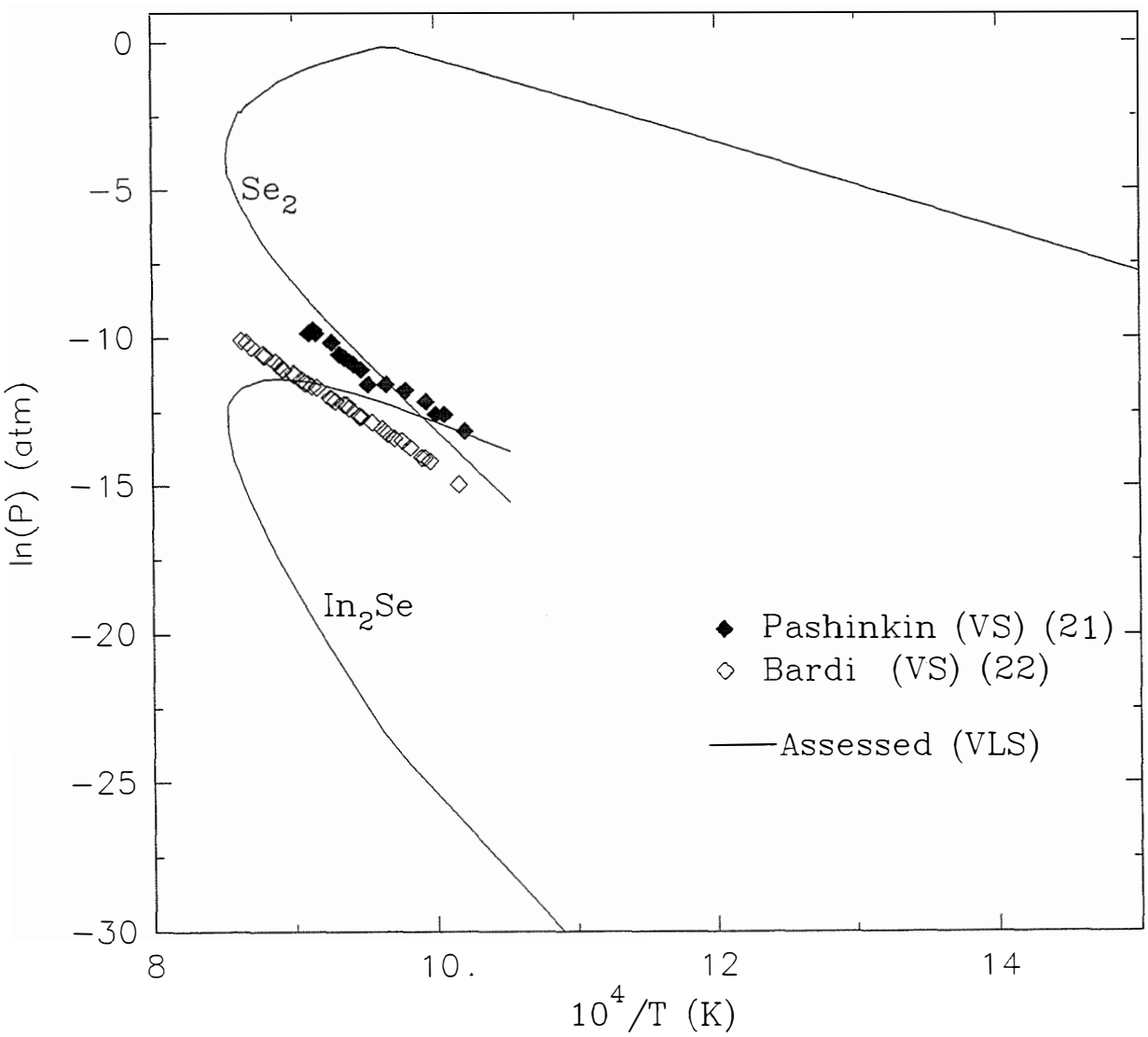

Figure 16. Equilibrium $In_2Se(g)$ and $Se_2(g)$ partial pressure over $In_2Se_3(s)$

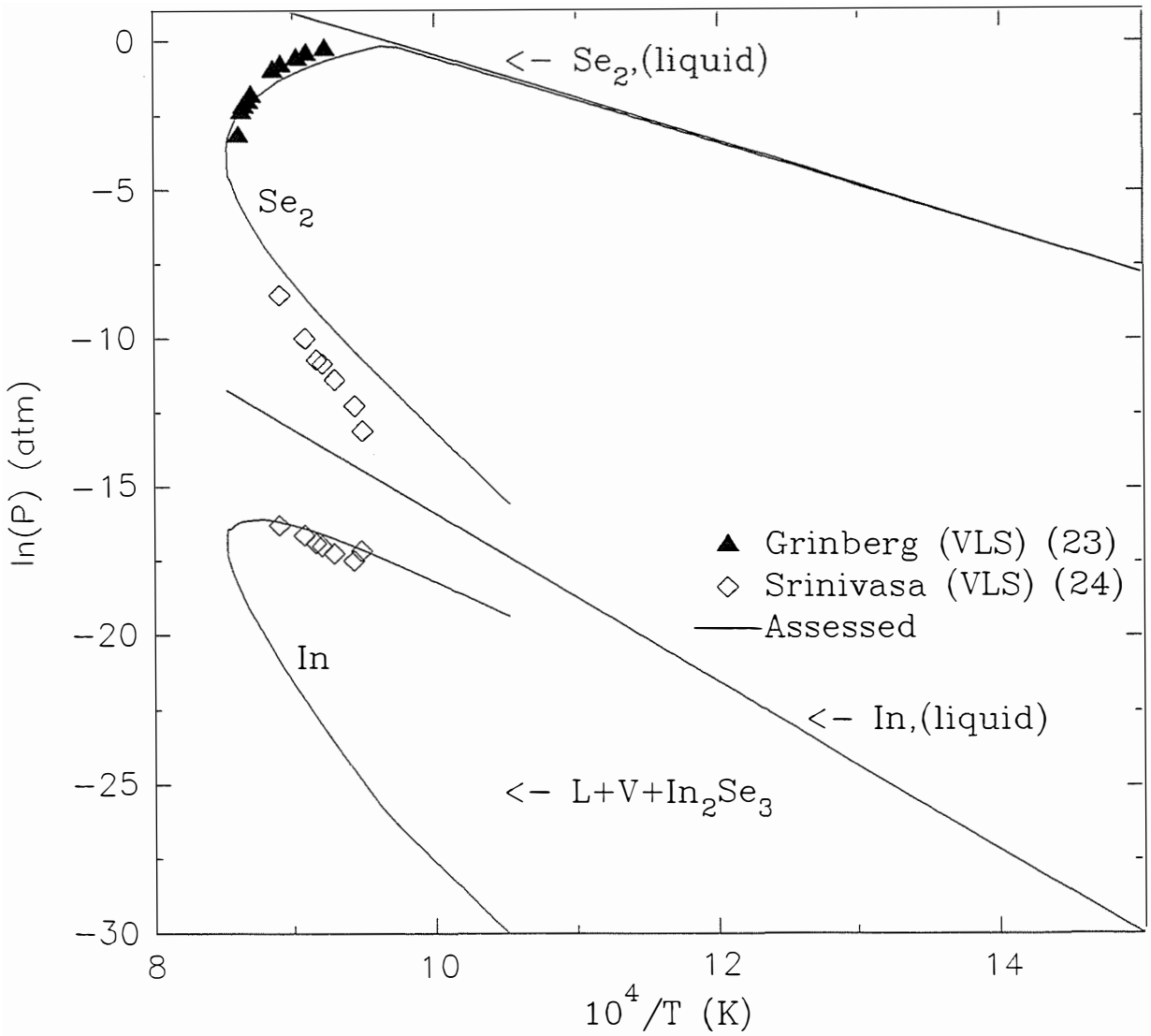

Figure 17. Equilibrium Se_2 and In partial pressure over In_2Se_3(s) liquidus

Another way to view these diagrams is to ask the question: What phases are present at a given temperature and fixed Se partial pressure? This is termed a predominance diagram and the calculated one for In-Se is shown in Figure 18. This diagram predicts that In_2Se_3 is the most stable condensed phase under typical processing temperatures at reasonable Se overpressures.

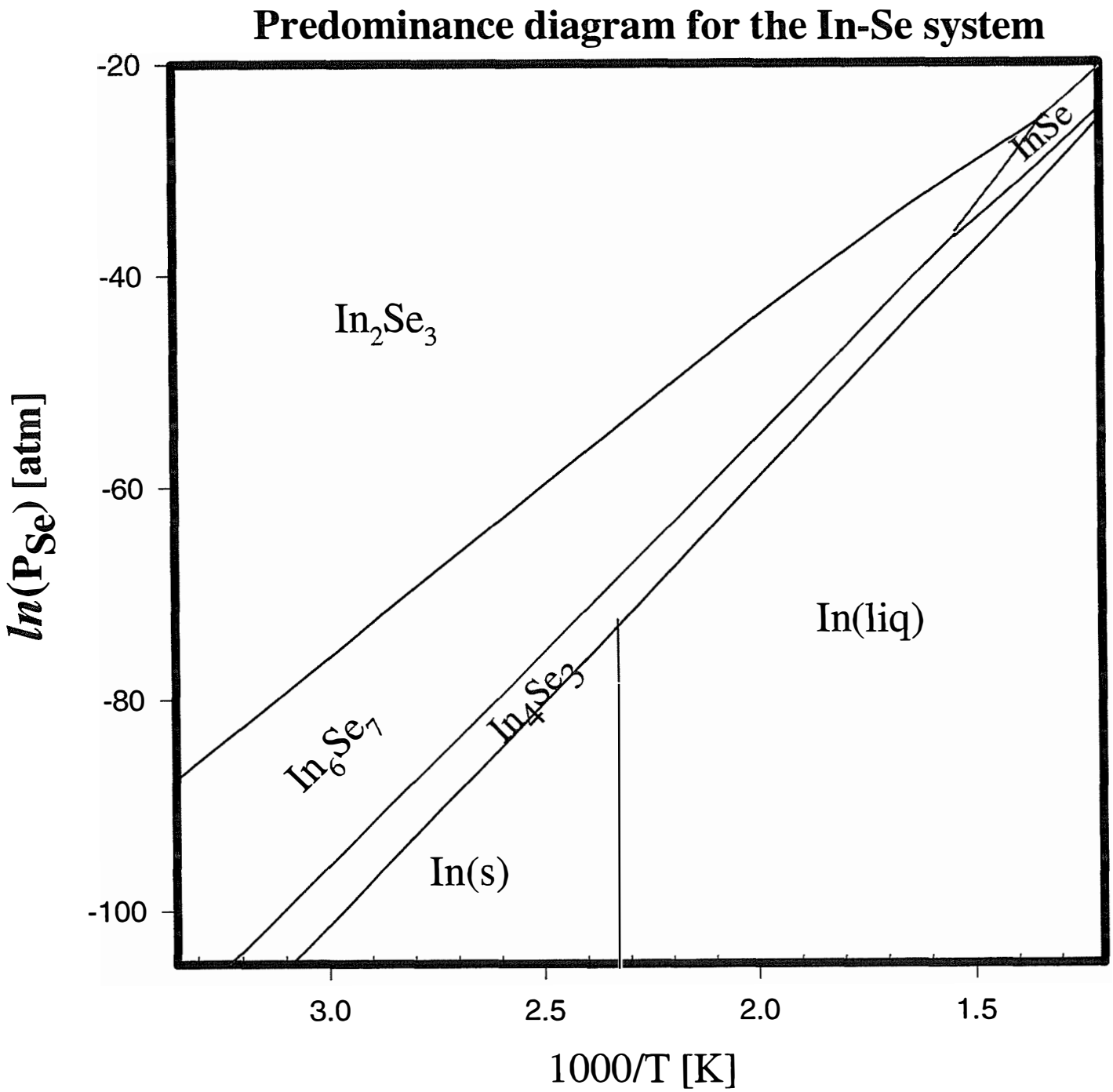

Figure 18. Predominance diagram for the In-Se system

(2) Experimental Studies

As shown in Figure 15, an inconsistency exists between the experimental liquidus data for In-rich solutions and the assessed phase diagram. The liquidus temperature corresponds to the conditions of equivalent component chemical potential (In or Se) in the liquid solution and the second equilibrium phase (solid compound or second liquid phase). When experimental liquidus temperature data are combined with both compound Gibbs energy data and liquid solution excess Gibbs energy data, the system is overdefined and true consistency tests can be performed. The difficulty in attaining a critical assessment of this system is the lack of data on the thermodynamic behavior of the liquid solution. For this reason it was decided to pursue an experimental determination of the liquid solution thermochemistry.

Solid state galvanic cells were used to determine the indium activity, a_{In}, in the composition range $0.10 < x_{Se} < 0.65$ and the temperature range 800 to 975 K. The cell configuration used in this study is represented as

$$W|In(\ell),In_2O_3(s)\|YSZ\|In_2O_3(s),In-Se(s \text{ or } \ell)|C|W$$

where YSZ is the solid electrolyte yittria stabilized zirconia. The open circuit EMF of this cell is directly related to the activity of In through the expression

$$\ell n[a_{In}] = 3FE/RT \tag{4}$$

where F is the Faraday constant, R the gas constant, and E the open circuit potential. In addition to providing information on the a_{In}, phase transition temperatures are apparent from changes in the slope of the open circuit potential as a function of temperature.

The experimental In-Se phase diagram shows a liquid-liquid miscibility gap extending from $0.05 \leq x_{Se} \leq 0.30$ at the monotectic temperature 793 K. The measured values of a_{In} at 800 and 900 K are shown in Figure 19 as a function of the overall Se mole fraction in the working electrode. These data indicate a value of $a_{In} = 0.96$ for $x_{Se} = 0.10$, 0.15, 0.20 and 0.25, consistent with a liquid-liquid miscibility gap. The measurement at $x_{Se} = 0.30$, however, produced a value $a_{In} = 0.91$, suggesting a narrower extent of the miscibility gap. At the higher temperature of 900 K, only the electrode compositions for $x_{Se} \leq 0.20$ gave a constant cell potential, which is consistent with the assessed phase diagram. The data indicate that positive deviations from ideal solution

behavior are present for In-rich compositions ($x_{In} \geq 0.7$), but negative departures are exhibited at higher Se contents.

For electrode compositions $x_{Se} > 0.30$, In and Se shots were encapsulated in evacuated fused silica ampoules, and long-time anneals at 650 K were performed to ensure equilibrium formation of the two-phase mixture. Eight compositions were formulated in the range $0.36 < x_{Se} \leq 0.65$ and analyzed by powder XRD. According to the reported phase diagram, the compositions x_{Se} = 0.36 and 0.42 lie in the same 2-phase field below the peritectic temperature (825 K). The data in Figure 19 confirm this phase relation (a_{In} = 0.91 at 800 K for both compositions) and the experimental peritectic temperature determined from the break in the emf vs temperature scan is 846 K. Figure 20 compares the measured transition temperatures with the assessed phase diagram and good agreement is apparent.

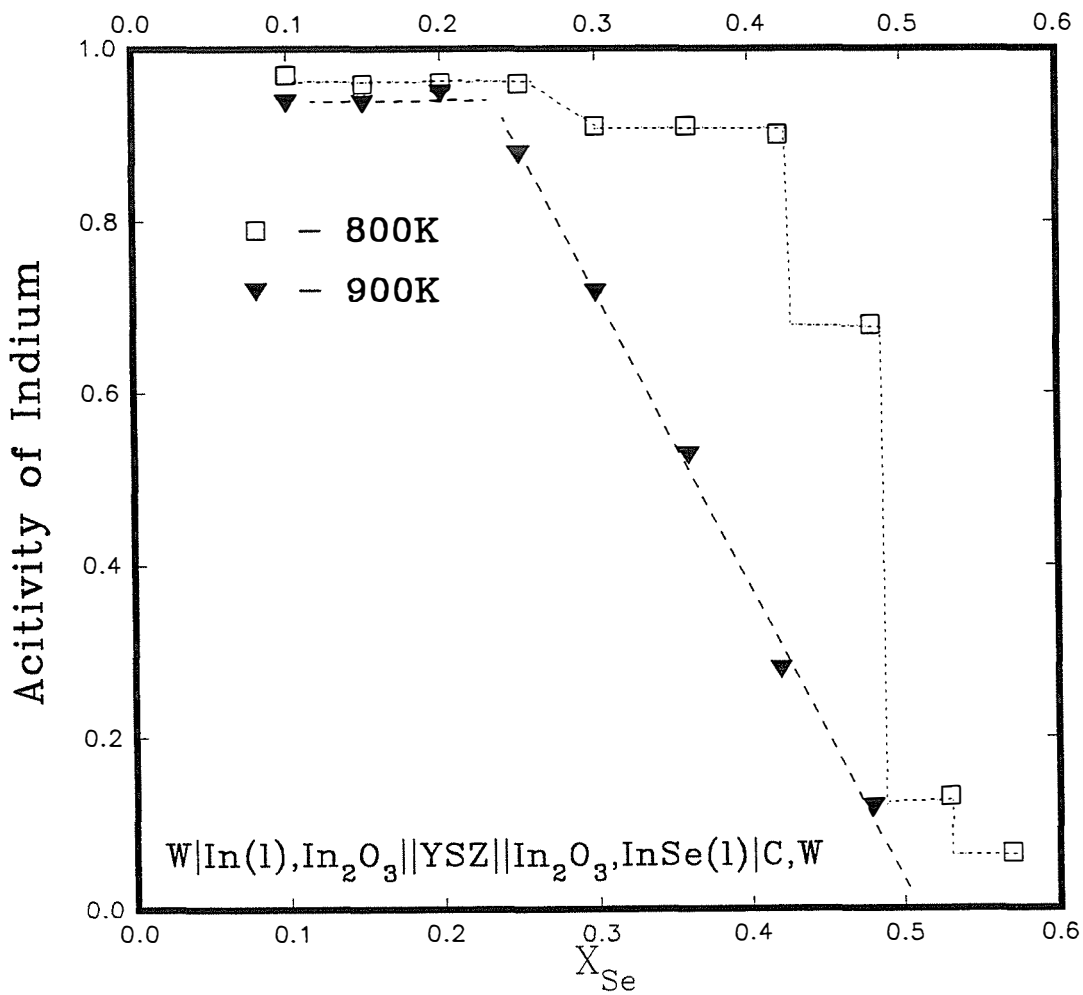

Figure 19. Experimental determination of the indium activity in In-Se melts with solid-state galvanic cells

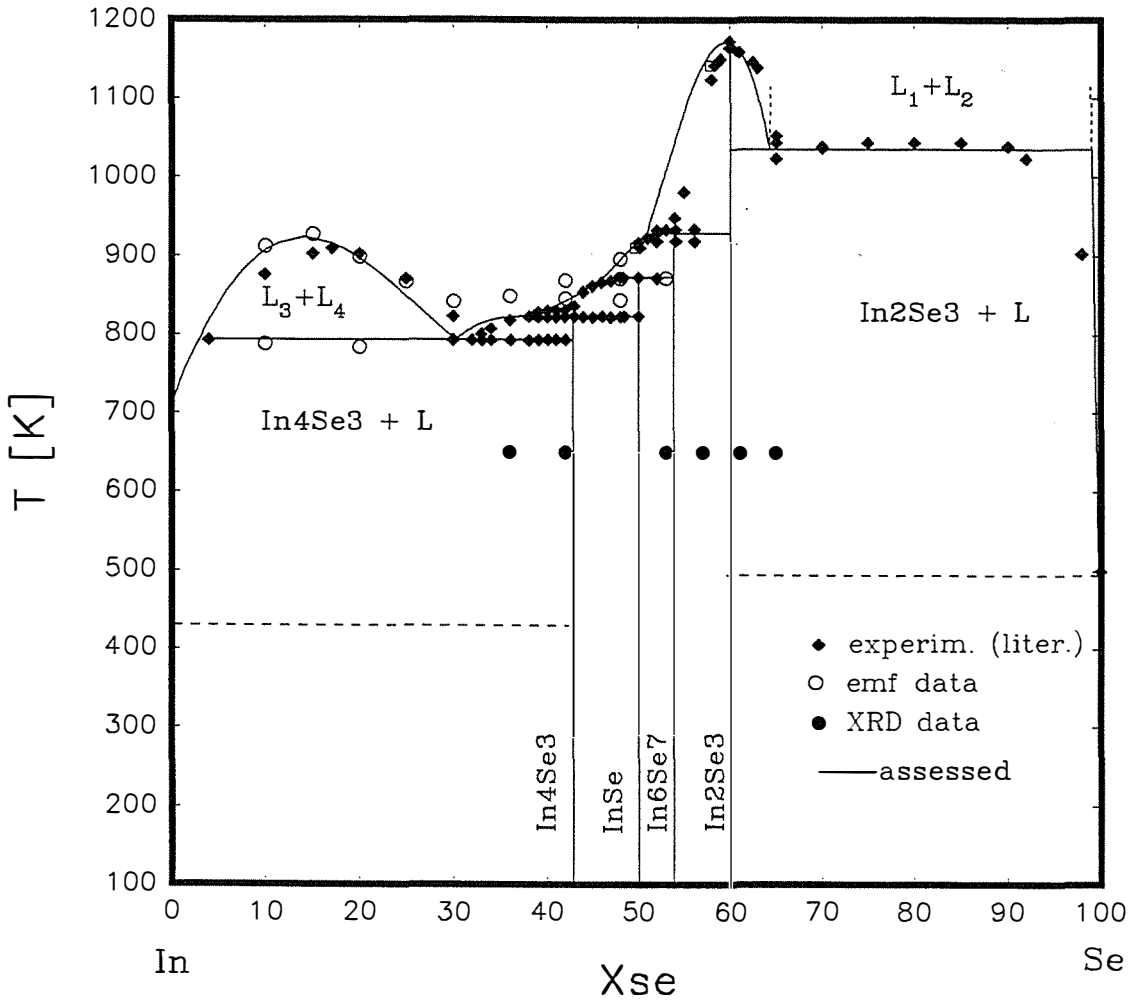

Figure 20. Assessed T-x phase diagram for In-Se system

Each experiment was repeated with a varying amount of In_2O_3 added to the working electrode and reproducible results were obtained for each electrode composition, except $x_{Se} = 0.61$ and 0.65. The measured emfs for the cells with a working electrode of these latter two compositions were much lower than the expected values and not reproducible. Analysis of the electrode compositions after each experiment suggested that Se from the working electrode had transported to the reference electrode to reduce the open circuit potential. An attempt was made to encapsulate the working electrode with B_2O_3 but reproducible results were not found.

Since meaningful results were not obtained at high Se contents, it was not possible to directly measure the Gibbs energy of formation of the intermediate compounds. If the literature data for

$\Delta G_f^o(In_4Se_3)$ is assumed correct, however, expressions for $\Delta G_f^o(InSe,\ In_6Se_7,$ and $In_2Se_3)$ can be obtained from the measured emf. The expressions are as follows:

$$\Delta G_f^o(InSe) = -144.8 + 6.045 \times 10^{-2} T(K),\ \pm 0.2 kJ/mol (798\ \text{to}\ 839K) \quad (5)$$

$$\Delta G_f^o(In_6Se_7) = -1{,}009.9 + 0.4351 T(K),\ \pm 1.6 kJ/mol (788\ \text{to}\ 862K) \quad (6)$$

$$\Delta G_f^o(In_2Se_3) = -447.4 + 0.2178 T(K),\ \pm 0.7 kJ/mol (786\ \text{to}\ 865K) \quad (7)$$

The value given by the last expression at 610 K, $\Delta G_f^o(In_2Se_3)$ = -314.5 kJ/mol, is in poor agreement with value reported by Mustafayev et al. [25], $\Delta G_f^o(In_2Se_3)$ = -201.3 kJ/mol, obtained by a molten salt emf method. To check consistency, a third law analysis was performed on the data used to derive expressions (5) and (7). The third law values $\Delta H_{f,298}^o(InSe)$ = -119.3 and $\Delta H_{f,298}^o(In_2Se_3)$ = -344.6 kJ/mol using the Gibbs energy data from this study are in excellent agreement with the values -117.0 and -344.0 kJ/mole reported by Hahn and Burrow [26] using combustion calorimetry.

These measurements have contributed significantly to the In-Se database and we plan to perform differential thermal analysis on the synthesized alloy compositions to verify the invariant and liquidus temperatures measured by the emf experiments. These data will then be included in the assessment procedure to yield a final assessment of the In-Se phase diagram. With the results of this assessment, reaction-couple diagrams will be calculated and compared with experimental results. This information should lead to a better understanding of the reaction pathway of absorber layer formation from the precursor film.

In the process of confirming the phase constitution of the annealed alloys, a new phase was discovered. Phase identification, crystal structures and lattice constants of the known phases were determined by powder X-ray diffraction and the results are shown in Tables 10 and 11.

The diffraction pattern of the sample $x_{Se} = 0.57$ revealed reflection peaks that did not correspond to any known phase. This implies the formation of a new compound and further analysis is needed to identify the compositional and thermal stability and the crystal structure of this phase.

Table 10. Phase analysis in annealed In-Se alloys.

x_{Se}	Phases Present
0.36	In_4Se_3 + InSe
0.42	In_4Se_2 + InSe + In (trace)
0.48	In_4Se_3 + InSe
0.53	InSe + In_6Se_7
0.57	In_2Se_3 + new
0.61	In_2Se_3 + Se
0.65	In_2Se_3 + Se

Table 11. Lattice structures of the compounds identified in the In-Se system.

Compound	Crystal System	Lattice Type	Lattice Parameters
In_4Se_3	To Be Determined		
InSe	Rombohedral (Hex.)	R3m	a=3.995 ± 0.004 c=16.60 ± 0.001
In_6Se_7	Monoclinic	P21	a=9.406 ± 0.010 b=4.051 ± 0.003 c=18.268 ± 0.020 β=109.01 ± 0.09
New-Phase	To Be Determined		
In_2Se_3	Hexagonal	P63/mmc	a=7.096 ± 0.04 c=19.28 ± 0.01

Cu-Se Binary System

The phase diagram for the Cu-Se system includes a liquid phase which exhibits two miscibility gaps, one for Cu-rich compositions and the other on the Se-rich side of the phase diagram. Four intermediate phases were reported in the literature, including the $Cu_2Se/Cu_{2-x}Se$, Cu_3Se_2, CuSe, and $CuSe_2$ phases. The $Cu_2Se/Cu_{2-x}Se$ phase was the most stable phase in this system with a broad homogeneity range extending to the Se side to form a defect compound. Extensive work has been conducted to clarify the Cu-Se phase diagram by means of DTA, X-ray, microscopy and microhardness techniques. These data are in qualitative agreement. Chakrabarti and Laughlin [27] reviewed the phase diagram and thermodynamic data for the system, but did not perform an optimized assessment.

We have performed a preliminary assessment of the Cu-Se system using the Redlich-Kister model to describe the liquid phase behavior. Four intermediate solid phases (Cu_2Se, Cu_3Se_2, CuSe, $CuSe_2$) were modeled as line compounds. Experimental data for $\Delta H^{\circ}_{f,298}$ and S°_{298} are available for each compound. Only the heat capacity data for Cu_2Se, however, are available in the literature. The heat capacities for Cu_3Se_2, CuSe, and $CuSe_2$ were estimated using the Unäl-Kubaschewski's rule [28] and corrected by applying the same rule to Cu_2Se. The resulting data were assigned uncertainties and the BINGSS routine [1] was used to optimize parameters. Excellent agreement between the assessed and experimental phase diagram was found, as shown in Figure 21. Four line compounds were included with only Cu_2Se melting in a congruent fashion (1393.5 K). The vapor species in equilibrium with the condensed phases in the Cu-Se system are Cu(g), Se_n(g), CuSe(g), and Cu_2Se(g), with Se_2(g) the most prominent species. The assessed Se_2 partial pressure in equilibrium with the liquidus, Cu_2Se, CuSe, and $CuSe_2$ was calculated and good agreement was apparent between the calculated T-p curve and the experimental data [29].

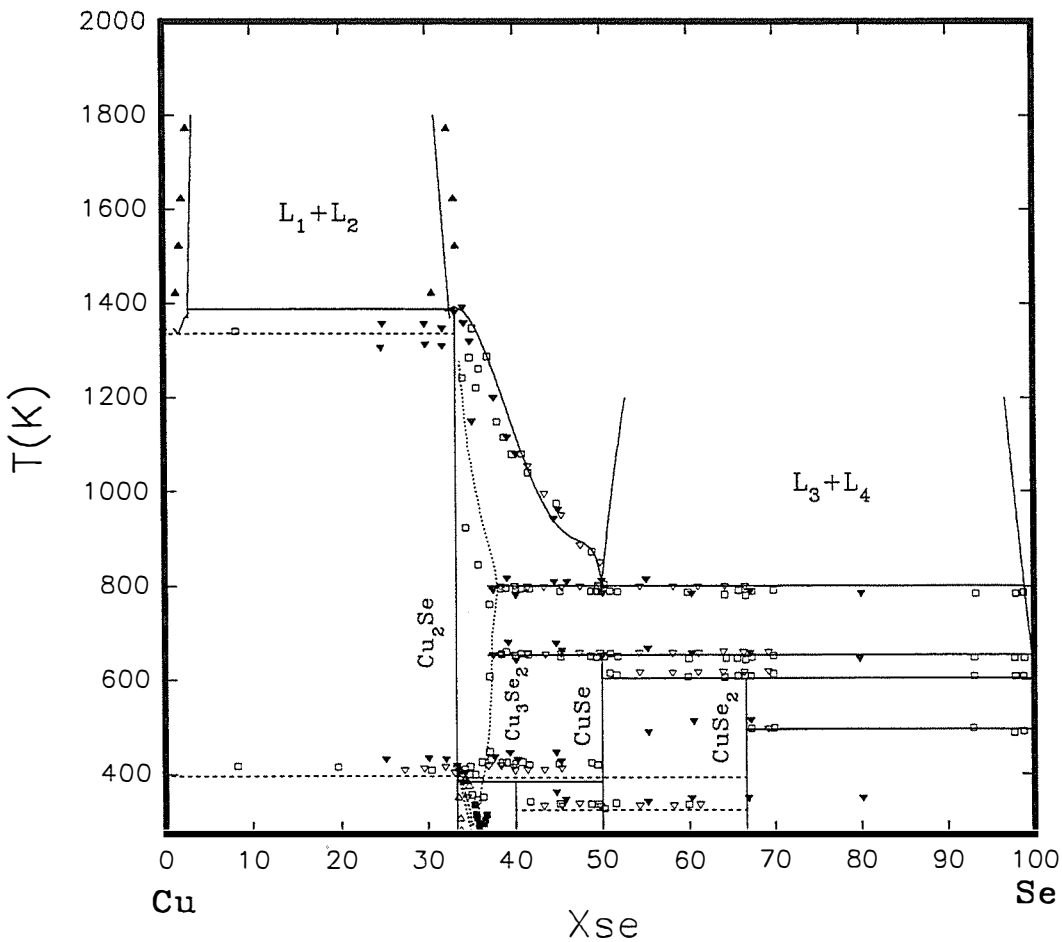

Figure 21. Assessed Cu-Se temperature-composition phase diagram

Summary

A critical assessment of the thermochemical and phase diagram data for the Cu-In-Se system using standard CALPHAD procedures has been initiated with an examination of the Se unary, and the binary In-Se, and Cu-Se systems. The results of this assessment have been applied to calculation of the flux characteristics of Langmuir cells for selenium evaporation, and to the engineering of precursor films for CIS synthesis. The next steps in this process will be the critical assessment of the Cu_2Se-In_2Se_3 pseudobinary section and the union of the three binary assessments to predict the phase relations along alternative binary tie-lines in the ternary phase field. Experimental studies of the phase diagrams and liquid mixture behaviors in the Cu-In-Se system are also underway in our laboratory. These experiments will test the assessment and substantiate the database used in the optimization.

References

[1] H.L. Lukas and G.B. Fries, *J. Phase Equilibria*, **13**, 532 (1992).

[2] B. Sundman, *ThermoCalc User's Guide*, (Stockholm, Sweden, 1995).

[3] L.E. Dodd. *J. Am. Chem. Soc.*, **42**, 1579 (1920).

[4] K. Neumann and E. Lichtenberg, *Z. Phys. Chem.*, **184**, 89 (1939).

[5] K. Niwa and Z. Shibata, *J. Fac. Sci.*, Hokkaido Univ., Ser. 3, **3**, 53 (1940a).

[6] R. Yamdagni and R.F. Porter, *J. Electrochem. Soc.*, **114**, 1021 (1957).

[7] H. Keller, H. Rickert, D. Detry, J. Drowart and P. Goldfinger, *Z. Physik. Chem.* (Neue Folge), **75**, 273 (1971).

[8] G. Preuner and J. Brockmöller, *Z. Phys. Chem.*, **68**, 157 (1910).

[9] H. Rau, *J. Chem. Therm.*, **6**, 525 (1974).

[10] E.H. Baker, *J. Chem. Soc. (London)*, **A**, 1089 (1968).

[11] J.Y.K. Huang, P.W. Gilles and J.E. Bennett, *High Temp. Sci.*, **17**, 109 (1984).

[12] J. Drowart, S. Smoes, A.M. Vander Auwera-Mahieu and E. Trio, *Proc. 3rd Int'l Symp. Industrial Uses of Se and Te*, Saltsjöbaden, Sweden (1984).

[13] G.K. Slavnova, N.P. Luzhnaya and Z.S. Medvedeva, *Russ. J. Inorg. Chem.*, **8**(5), 78 (1963).

[14] A. Likforman and M. Guittard, *Compt. Rend. (Paris) C*, **279**, 33 (1974).

[15] K. Imai, K. Suzuki, Y. Hazegawa and Y. Abe, *J. Crystal Growth*, **54**, 501 (1981).

[16] A.T. Dinsdale, *CALPHAD*, **15**, 317 (1991).

[17] G.K. Slavnoova, N.P. Luzhnaya and Z.S. Medvedeva, *Russ. J. Inorg. Chem.*, **8**(5), 622 (1963).

[18] K. Imai, K. Suzuki, T. Haga, Y. Hasegawa and Y. Abe, *J. Crystal Growth*, **54**(3), 501 (1981).

[19] T. Okada and S. Ohon, *J. Phys. Soc. Jpn.*, **62**(5), 1669 (1993).

[20] V.M. Glazov, S.G. Kim and K.B. Nurov, *Inorg. Mater.*, **25**(5), 727 (1989).

[21] A.S. Pashinkin, Vl. V. Zharov, *Inorg. Mater.*, **24**(9), 1458 (1988).

[22] G. Bardi, V. Piacente and P. Scardala, *High Temp. Sci.*, **25**, 175 (1988).

[23] Ya. Kh. Grinberg, V.A. Boryakova, V.F. Shevelkov and Z.S. Medvedeva, *Inorg. Mater.*, **8**, 2099 (1972).

[24] R.S. Srinivasa and J.G. Edwards, *J. Electrochem. Soc.*, **134**, 1811 (1987).

[25] F.M. Mustafaev, T.Kh. Azizov, I.Ya. Aliev and A.S. Abbasov, *Azerb. Khim. Zh.*, **2**, 93 (1974).

[26] H. Hahn and F. Burrow, *Agnew. Chem.*, **68**, 382 (1952).

[27] D.J. Chakrabarti and D.E. Laughlin, *Bulletin of Alloy Phase Diagrams*, **2**(3), 305 (1981).

[28] O. Kubaschewski and H. Unäl, *High Temp. High Pressure*, **9**, 361 (1977).

[29] H. Rau and A. Rabenau, *J. Sol. St. Chem.*, **1**, 515 (1970).

CELL FABRICATION INFRASTRUCTURE DEVELOPMENT

To meet the science and technology goals of this project, a cell fabrication capability is being established at the University of Florida. Processing facilities include systems for depositing Mo, CIS precursor films, CdS, and ZnO. In addition, a capability to rapid thermally process precursor films has been demonstrated, as well as characterization techniques.

Plasma Migration Enhanced Epitaxy (PMEE)

A key component of our fabrication infrastructure is the plasma migration enhanced epitaxial deposition system. PMEE is a versatile process with respect to substrate choice and the element independent source arrangement permits excellent film stoichiometry control. The incorporation of an ECR plasma selenium source will reduce the deposition temperature, ensure efficient Se incorporation, and importantly, permit high deposition rates. The initial design and partial construction of this system was performed by B. Stanbery at Boeing and transferred to the University of Florida.

A schematic of the PMEE system is shown in Figure 22. CIS film growth will take place in a CHA SE-1000 diffusion-pumped LN_2-trapped baseplate system and feedthrough collar with a custom built stainless steel bell-jar built by MDC Vacuum Products Corporation. Inside is a rotating molybdenum disc substrate platen with a capacity of up to nine 3" diameter substrates rotating above both a dual filament EPI, Inc. copper effusion cell and EPI single modified filament indium effusion cell. Rate control is provided by a Leybold-Hereaus Inficon Sentinal III with both EIES sensors for monitoring and controlling the metals deposition process and quartz crystal oscillators for calibration. The system incorporates custom boron nitride-coated radiant heaters designed for operation to 1000°C and used for substrate temperature control. The design also includes both a load-lock and a cryoshroud for high selenium pumping speeds and improved source stability resulting from reduced thermal cycling of sources during sample changes. The reactor will simultaneously grow on up to nine substrates per run, each mounted on a separate, removable sample holder. The stainless steel water-jacketed chamber walls include ports with source

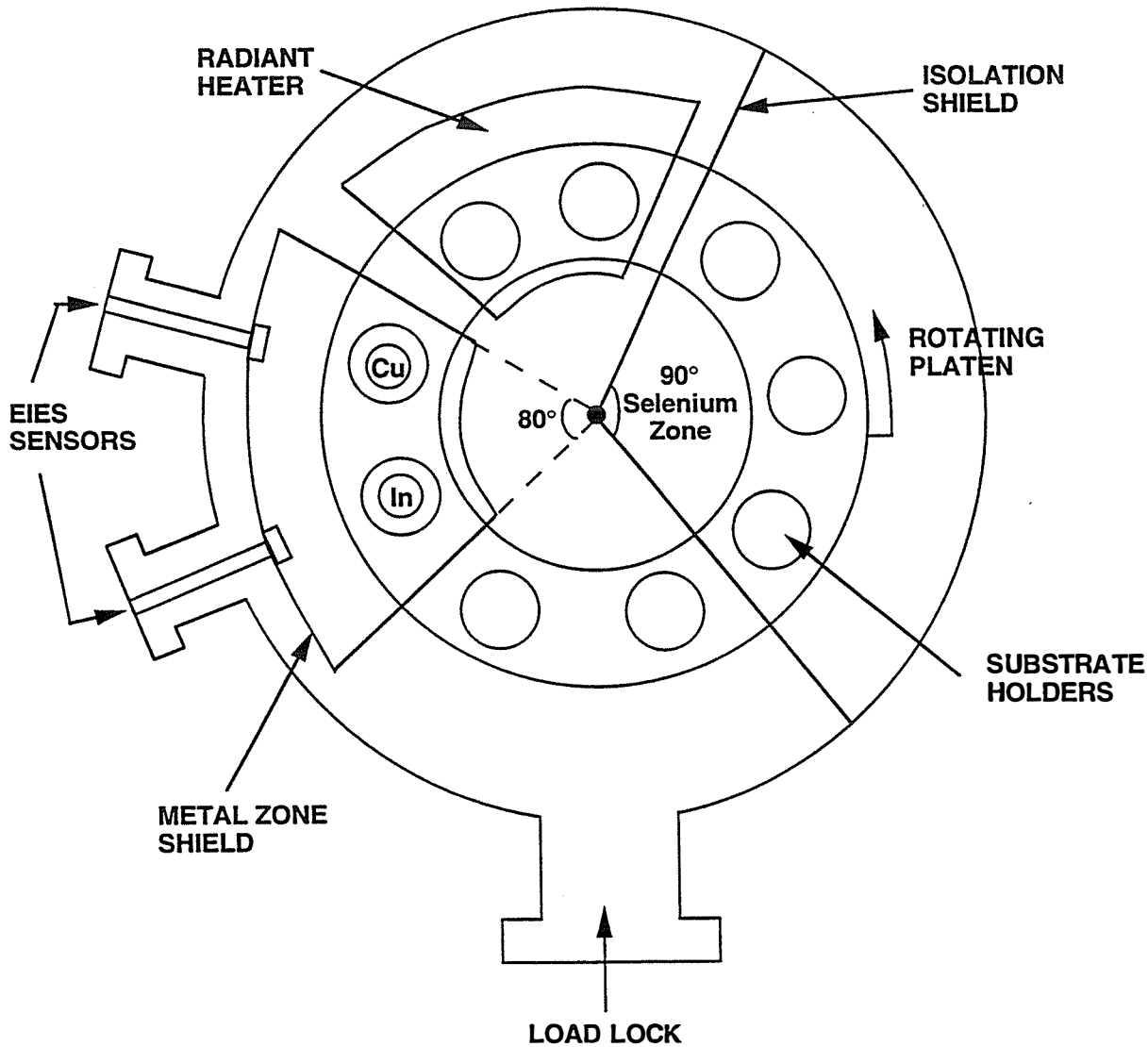

Figure 22. Schematic of the plasma migration enhanced epitaxy system

shutters for the copper and indium and includes a feedthrough adjacent to the plasma source designed specifically for an EPI, Inc. thermal cracking effusion cell with the beam coincident on the growth surface with the source beam for an ECR plasma cracker source for selenium. The latter is mounted onto a water-cooled baffle which further isolates the group VI sources from the metal evaporation sources. Microwave power is provided by an Astex S-250 power supply. The high purity gas delivery system to the ECR source includes a SemiGas Nanochem 3000 point-of-use gas purifier. A Leybold-Hereaus Quadrex 200 residual gas analyzer with a separate turbomolecular pump is attached to a load-lock port, and a Balzers QMG 420 is attached to the bell-jar directly above the plasma source (cross-beam configuration) for direct measurement of the ion flux mass distribution.

After overcoming a number of problems, including a leak in the pump stack, the system installation was completed at the end of the year. A base pressure in the 10^{-9} Torr range was achieved and initial calibration runs were completed.

CdS Deposition

Both chemical bath deposition (CBD) and metalorganic chemical vapor deposition (MOCVD) of CdS were demonstrated during the past year. The CBD process was an adaptation of that developed at Boeing and used NH_3, NH_4Cl, $CdCl_2$ and NH_2CSNH_2 reagents at 80 to 85°C in a well-stirred bath to deposit CdS. Initially there was difficulty with pin-hole formation, but reproducible films can now be grown. The films were characterized by profilometry, optical absorption spectroscopy, microscopy, and FTIR and found to be uniform in thickness, compact, coherent, and colloid-free.

A dry process was also demonstrated using an existing MOCVD system. This system incorporates a run-vent manifold in an atmospheric pressure, horizontal reactor design. The gas delivery manifold and gas clean-up segments were constructed by Spire, while the reactor was designed at the University of Florida. One of the issues associated with MOCVD of CdS for CIS-PV applications is the requirement of low temperature deposition to preserve the integrity of the underlying CIS film. It was established that the use of $Cd(CH_3)_2$ and H_2S as precursors in a molar ratio 1/100 permitted CdS to be deposited at 160°C at a reasonable rate. These films were also of good quality. As discussed in the first section of this report, the MOCVD grown CdS produced films with improved excess carrier lifetimes.

Sputter Deposition of Mo and ZnO

As a first step in the fabrication of a cell, a thin Mo film is typically deposited on float processed soda-lime glass substrates. Although the further development of Mo film deposition is not a specific objective of this project, the quality of the Mo layer will certainly influence the results of subsequent processing.

Mo films were deposited in a diffusion pumped/cryotrapped sputter system, using 2" diameter planar magnetron sputter guns (US Guns Inc). A US MDX-1K DC power supply was used to generate the plasma in an ultrahigh purity argon gas flow. A throttle valve was used to modulate the chamber pressure, which was measured by thermocouple gauges and MKS Baratron capacitance manometer. A substrate heating system, using vacuum compatible resistive

elements, was also installed. The substrate temperature was monitored with a thermocouple attached to the substrate holder in close proximity to the resistive heating assembly. A range of growth parameters was explored, including gas pressure, input power, and substrate temperature. Construction of a substrate holder to accommodate 12 substrates was completed to satisfy a large demand for Mo-coated substrates.

A number of characterization tools were used in the analysis of the Mo thin films, including X-ray diffraction, AFM, profilometry, four point probe, and the "scotch tape" test. X-ray diffraction results indicated that BCC Mo films were deposited with a preferred texture of (110) parallel to the surface. AFM was used to analyze the surface morphology of the films, determine the grain size, and identify surface imperfections. An example AFM micrograph is shown in Figure 23. Computer analysis determined a mean surface roughness of 2.76 nm, with maximum height deviations of 22.9 nm for a 1 μm x 1 μm area of surface. The average grain diameter was estimated to be 0.1 μm.

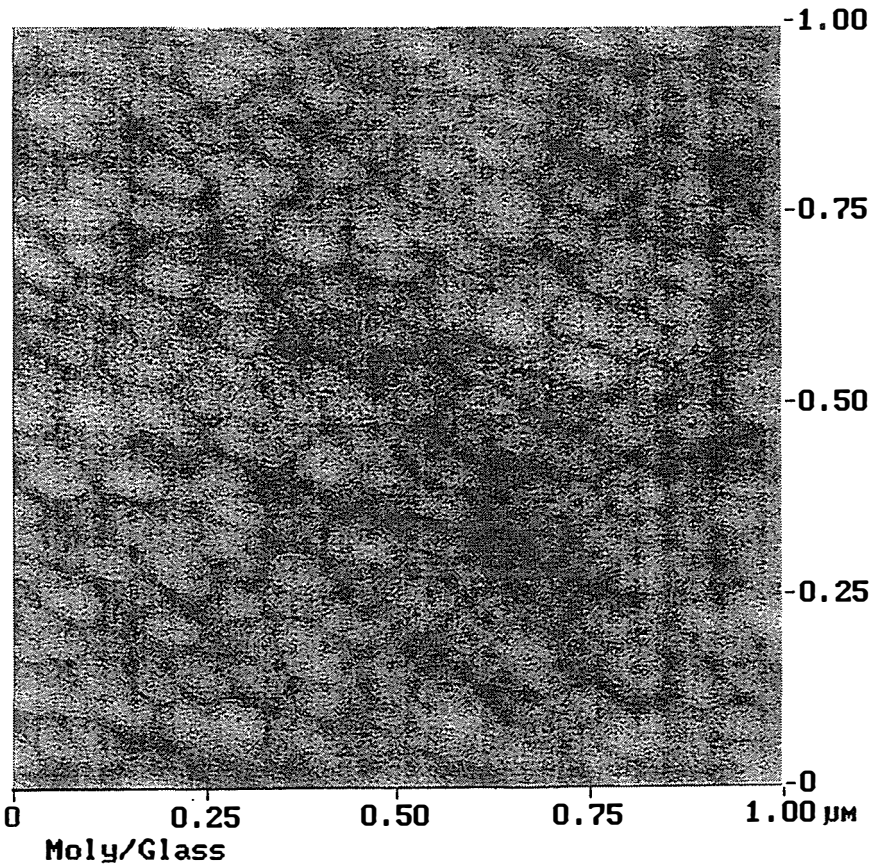

Figure 23. AFM micrograph of sputtered Mo film on glass

Four point probe measurements were used to determine the film resistivity. The literature suggests that the Mo film should be at least 1 μm thick to achieve low resistance and film stress. Measured resistivities of the order of ~8 x 10^{-5} Ω-cm were achieved, which is approximately an order of magnitude greater than the reported bulk value (~8 x 10^{-6} Ω-cm). It was found that film adhesion is improved by substrate heating. This was demonstrated by depositing 2 films with the same sputter parameters, with one sample deposited at room temperature, and the other at 150°C. The sample heated to 150°C exhibited no peeling, whereas the room temperature sample delaminated. Future analysis of the films will use a modified Tencor Flexus FLX-2320 thin film stress analysis optical reflectometer. This system uses a dual wavelength laser to measure curvature of a substrate, which can be related to the film stress. Modifications to this system have just been completed to make it compatible with the 2" x 2" SLG substrates.

One of the objectives of this research program is to explore alternative methods for depositing the transparent conducting oxide (TCO) "window" layer. Specifically, we are exploring DC sputtering of ZnO from metallic Zn targets using boron and silicon doping. To this end, films of ZnO were prepared using the same sputter system as used to deposit the Mo films. The only hardware modification was the use of US GUN RF planar magnetron sputter source. An argon ambient at approximately 12 mTorr was used and input power was 100 W. To gain experience in ZnO sputtering an undoped ZnO target was first loaded into the system.

The deposited films were characterized by visual inspection, Auger electron spectroscopy, X-ray diffraction, profilometry, and four point probe. X-ray diffraction spectra revealed that the film structure was wurtzite with a preferred texture of the basal plane texture parallel to the surface. Auger electron spectroscopy verified that a ZnO film had been deposited. Measurements of the compound stoichiometry from the weighted peak height analysis gave large uncertainties since the data was reduced without standards. Four point probe measurements were also attempted on the samples. Off stoichiometric ZnO films showed an intrinsic doping effect and subsequent lower resistivities, the value of which depended on the film stoichiometry; ZnO films with 1:1 stoichiometry were highly insulating.

Rapid Thermal Processing

Our approach to developing a high throughput CIS manufacturing process incorporates a 2-step precursor deposition process. In the first step a thin layer of large-grain, single-phase $CuInSe_2$ is deposited to act as a nucleation layer. This is followed by a high rate deposition of the bulk of the precursor film. The precursor phases will then be reacted by rapid thermal processing (RTP)

to obtain large-grain, single-phase $CuInSe_2$ throughout the film with the desired surface phase. In addition to optimizing the precursor film characteristics, the RTP conditions (e.g., ramp rate, soak time, ambient vapor) also will need optimized. As part of our first year activities, a RTP facility has been established.

A schematic of the custom RTP system is shown in Figure 24. As shown in this figure, the sample is heated from above and below by banks of tungsten-halogen lamps. Both air and water cooling are provided to permit rapid temperature adjustment using a Micristar 5280 PID programmer/controller. A silicon carbide-coated graphite susceptor was designed that included multiple source wells to provide an overpressure during processing. The susceptor's cavity was designed sufficiently deep to allow processing with a proximity cap. The system has been constructed and tested with Mo/glass and Cu/Se/Mo/glass samples.

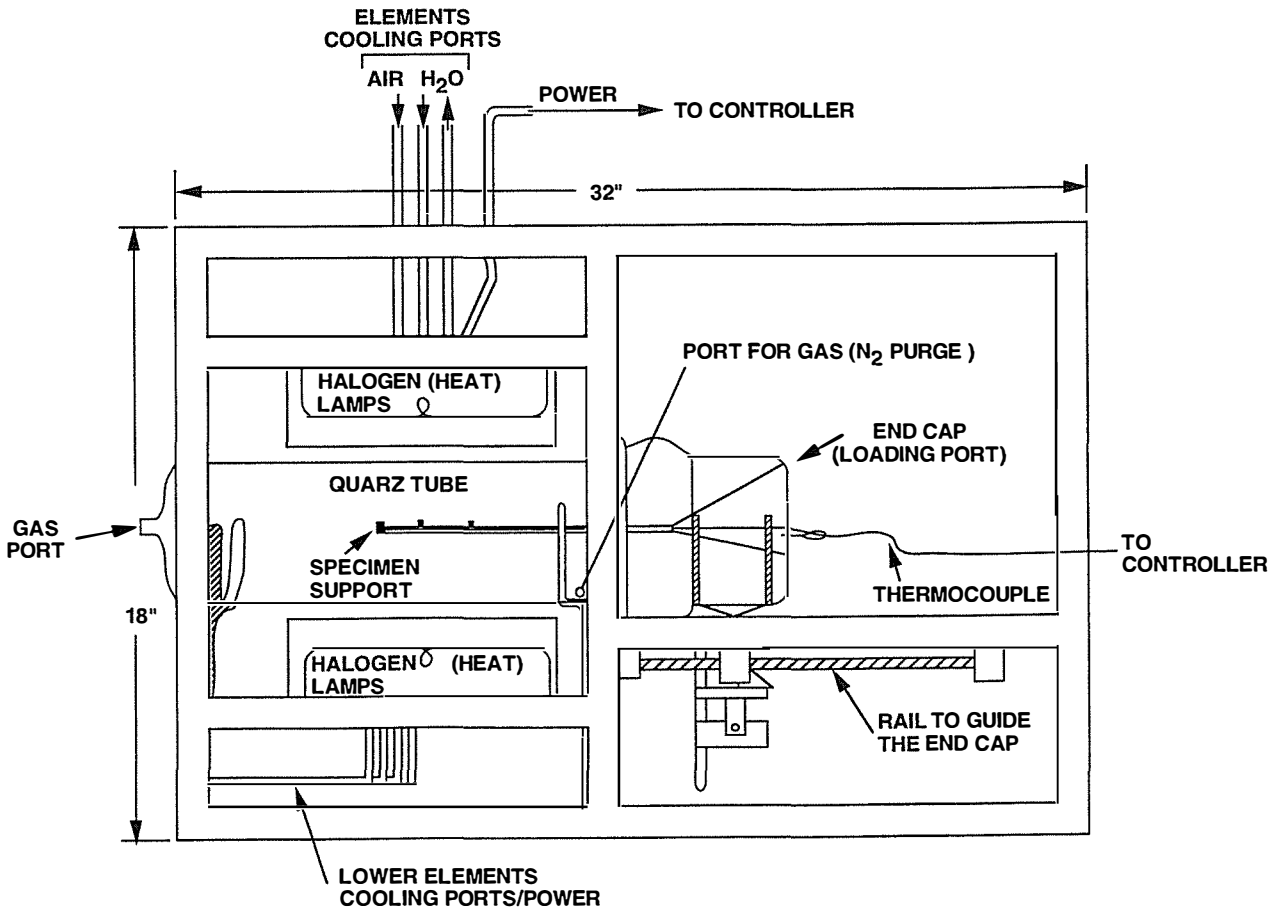

Figure 24. Schematic of the rapid thermal processing system

TEAM ACTIVITIES

The interdisciplinary University of Florida research team funded by this contract has been consistently active in the TFPP teaming activities during the entire first phase of the program. In addition, collaborative research has been initiated under the auspices of the DOE Basic Energy Sciences Division.

TFPP Team Participation

During Phase I, Professors Anderson and Sheng Li along with Billy Stanbery have attended team meetings and participated actively in the CIS Junction Team's goal of developing a better understanding of the effects of buffer layer processing on CIS device performance. The Junction Team's second principle goal of investigating non-destructive quality assessment techniques has been simultaneously pursued by means of the vigorous application of our unique DBOM measurement capability.

As discussed at length in preceding sections of this report, we have characterized samples from NREL, USF and IEC both with and without buffer and window layers. We have also published the results of buffer layer processing experiments conducted on high-quality NREL CIGS (see Communications section) which complement those conducted by NREL and further our understanding of the complex interactions between buffer layer processing and CIGS films. These collaborative activities were undertaken in support of the TFPP Junction Team's goals and unequivocally established the usefulness and relevance of the simple, noncontact, nondestructive DBOM technique.

BES Activity

During Phase I a collaborative research relationship was established between UF and Dr. Richard Anderson at Sandia Livermore Laboratories. We have agreed to work together to apply their extensive optical measurement capabilities to investigation of the effects of disorder in CIS materials on carrier transport properties. As is always the case in such exploratory basic research

their exists the potential for uncovering other unexpected information as well. We anticipate results from this collaboration during the second phase of this contract.

COMMUNICATIONS

1. "Effects of Buffer Layer Processing on CIGS Excess Carrier Lifetime: Application of Dual-Beam Optical Modulation to Process Analysis," S.S. Li, B.J. Stanbery, C.H. Huang, C.H. Chang, Y.S. Chang and T.J. Anderson. Presented at 25th IEEE Photovoltaics Specialists Conf., May 13-17, 1996 (Washington, DC).

2. "Thermodynamic Assessment of the Cu-In-Se System and Application to Thin Film Photovoltaics," C.H. Chang, A. Davydov, B.J. Stanbery and T.J. Anderson. Presented at 25th IEEE Photovoltaics Specialists Conf., May 13-17, 1996 (Washington, DC).

REPORT DOCUMENTATION PAGE

Form Approved
OMB NO. 0704-0188

Public reporting burden for this collection of information is estimated to average 1 hour per response, including the time for reviewing instructions, searching existing data sources, gathering and maintaining the data needed, and completing and reviewing the collection of information. Send comments regarding this burden estimate or any other aspect of this collection of information, including suggestions for reducing this burden, to Washington Headquarters Services, Directorate for Information Operations and Reports, 1215 Jefferson Davis Highway, Suite 1204, Arlington, VA 22202-4302, and to the Office of Management and Budget, Paperwork Reduction Project (0704-0188), Washington, DC 20503.

1. AGENCY USE ONLY (Leave blank)	2. REPORT DATE	3. REPORT TYPE AND DATES COVERED
	April 1997	Phase I Annual Report, 6 May 1995 - 5 May 1996

4. TITLE AND SUBTITLE

Processing of $CuInSe_2$-Based Solar Cells: Characterization of Deposition Processes in Terms of Chemical Reaction Analyses; Phase I Annual Report, 6 May 1995 - 5 May 1996

5. FUNDING NUMBERS

C: XAF-5-14142-10
TA: PV704401

6. AUTHOR(S)

T. Anderson

7. PERFORMING ORGANIZATION NAME(S) AND ADDRESS(ES)

Department of Chemical Engineering
University of Florida
Gainseville, FL 32611

8. PERFORMING ORGANIZATION REPORT NUMBER

9. SPONSORING/MONITORING AGENCY NAME(S) AND ADDRESS(ES)

National Renewable Energy Laboratory
1617 Cole Blvd.
Golden, CO 80401-3393

10. SPONSORING/MONITORING AGENCY REPORT NUMBER

SR-520-22797

DE97000241

11. SUPPLEMENTARY NOTES

NREL Technical Monitor: B. von Roedern

12a. DISTRIBUTION/AVAILABILITY STATEMENT

12b. DISTRIBUTION CODE

UC-1260

13. ABSTRACT *(Maximum 200 words)*

This report describes work performed by the University of Florida during Phase I of this subcontract. Researchers developed a nondestructive, contactless, dual-beam optical modulation technique for measuring the excess carrier lifetimes and surface recombination velocities in $CuInGaSe_2$. They tested the method in both a reflectance and transmission mode and generated a model to interpret the data. Measurements on a sample in both modes gave measured lifetimes that agreed within experimental error. Researchers performed critical assessments of the Se unary and the In-Se and Cu-Se binary systems. The results of the Se assessment indicated that the dominant species are Se_2 for T> 1000K, Se_5 in the range 600<T<1000 K, and Se_6 for T<600 K. Equilibrium evaporation fluxes were estimated using the assessed thermochemical properties. Researchers also established a cell fabrication infrastructure. The plasma-migration-enhanced epitaxy system was transferred from Boeing, and initial calibration runs were performed. In addition, researchers installed and demonstrated a capability for radio frequency sputtering of Mo, chemical-bath deposition, metal-organic chemical vapor deposition of CdS, and rapid thermal processing of Mo/glass and Cu-Se/Mo/glass.

14. SUBJECT TERMS

photovoltaics ; $CuInSe_2$-based solar cells ; deposition processes ; characterization chemical reaction analysis

15. NUMBER OF PAGES
63

16. PRICE CODE

17. SECURITY CLASSIFICATION OF REPORT	18. SECURITY CLASSIFICATION OF THIS PAGE	19. SECURITY CLASSIFICATION OF ABSTRACT	20. LIMITATION OF ABSTRACT
Unclassified	Unclassified	Unclassified	UL